Optical characterisation of AAO/$CsPbBr_3$ perovskite nanocomposites

LUND UNIVERSITY

Klára Nováková

Department of Physics

Lund University

Thesis submitted for the degree of

Master of Science

Supervisor:

Ivan Scheblykin

Co-supervisors:

Jesper Wallentin

Eva Unger

Project Duration: 4 months

Divison of Synchrotron radiation

Division of Chemical Physics

January 2021

Abstract

Direct bandgap metal lead halide perovskites offer promising optoelectronic properties desirable in a wide range of applications including photodetection. However, the incomplete and poor understanding of the photophysical processes taking place in these materials, along with their poor stability, is the bottleneck for optimisation and further development of metal halide perovskite devices. In this work, we study all-inorganic $CsPbBr_3$ perovkite nanowires embedded in anodized aluminium oxide (AAO) template where samples with templates of different pore sizes, ranging from 30 - 360 nm, are optically characterised with photoluminescence spectroscopic techniques. Steady-state photoluminescence spectroscopy reveals a blue-shift in the emission wavelength with decreasing nanowire diameter beyond quantum confinement. The origin of such an effect remains ambiguous, however, the shift in wavelength is attributed to possible strain effects induced by the AAO matrix on the lattice structure of the nanowires. Time-correlated single photon counting unveils different charge carrier dynamics for smaller nanowire diameter, 30-170 nm, and larger nanowire diameter 250 - 360 nm samples. Here the longer charge carrier decay times of samples with smaller nanowire diameter suggest a trap-mediated radiative decay dynamics.

Popular Science

With the current digitisation and increasing living standards across the globe, the global electricity consumption is rapidly increasing. It is to no surprise that scientists from all over the world are constantly searching for more efficient energy solutions through explorations of new materials. For the last two decades, the material that holds the crown for the future saviour of the world is a perovskite crystal.

It is of course no ordinary crystal like that you find on a fancy engagement ring or in a box of salt. It is a crystal prepared in a lab where scientists are like chefs that can cook up countless different perovskite crystals with great amount of freedom from various elements of the periodic table. This almost magical crystal has excellent properties for solar cells, LED lamps, electronics and detectors of visible light or X-rays (which you take when you break a leg). The wide range of applications where perovkites are predicted to succeed even on the industrial market is given by the malleable character of the possible element composition and its semiconducting nature. But what does it mean to be a semiconductor?

It simply means that the material only conducts electricity sometimes and in a controllable manner. You can imagine the electronic structure of a semiconductor as two shelves above each other. The bottom shelf is full of billiard balls while the top is completely empty. The billiard balls in the bottom shelf sit so tightly that there can be no motion. Imagine now that the billiard balls are electrons and that the only way to move an electron from the bottom to the top shelf is by giving it an extra energy, let's say in the form of light. When a semiconductor receives this extra energy, its electrons jump from the bottom to the top shelf where the electrons can move freely and conduct electricity. After a while the electrons can fall back down to the bottom shelf but at the same time they need to give off the extra energy that got them up in the first place. One way to get rid off this energy is to covert it back to the form of light which has the same energy as, approximately, the

gap between these two shelves. The process of a semiconductor emitting light is called photoluminescence. The studies of the light emitted by the semiconductor can therefore reveal information about the material's electronic structure.

Now coming back to perovskites and their outstanding properties, even more attractive characteristics are seen for small perovskite rods which are 500 times thinner than human hair. We call these rods nanowires. To make the perovskite nanowires, we can use a template covered with many pores and let the nanowires grow in the pores. Given the unstable nature of perovskites, the template can act as a physical protection of the crystals as well. This work focuses exactly on these thin nanowires of a particular perovskite, cesium lead bromide ($CsPbBr_3$), grown inside different templates with varying pore sizes. The electronic structure of the samples with different nanowire diameters was studied by shining a laser on the sample and analysing the photoluminescence light coming out of the sample. Our photoluminescence study clarifies the dependence of the electronic structure of the perovskite crystal on the diameter size and investigates an ideal pore size for the application of the material in a future detector for X-rays. So who knows, maybe one day you will be leaving the hospital with an X-ray image made with a perovkite-based detector!

Acknowledgements

First and foremost, I would like to express my gratitude to my supervisor Ivan Scheblykin for his continuous support during the project both in the laboratory and during theoretical discussions. I would like to further thank my co-supervisors, Jesper Wallentin and Eva Unger for their virtual encouragement and addition of different perspectives to the consultations of the work. However, an additional special thank you goes to Eva for putting the project together and making it possible for me dive into the world of perovskites.

Moreover, I would like to thank my colleague Klara Suchan for introducing me to the laboratory set-up and giving me feedback and suggestions on my data analysis and my colleague Zhaojun Zhang for producing the samples and giving me insight into the preparation procedure. The experiments would also not have been possible without the help of my colleagues from the Single Molecule Spectroscopy group, Shraddha, Aymen, Bruce, Sudipta, Boris and Alex, who were always there to assist me to make any adjustments and fixes to the set-up and give me a general advice.

Klára Nováková
14^{th} December 2020

Acronyms and Abbreviations

0,1,2,3D 0,1,2,3 dimensional

AAO Anodized aluminium oxide

APD Avalanche photodiode

CB Conduction band

CCD Charge-coupled device

CMOS Complementary metal-oxide semiconductor

DMSO dimethylsulfoxide

FWHM Full width at half maximum

MHP Metal halide perovkite

LED Light emitting diode

LP Long pass

NW Nanowire

OD Optical density

PMT Photomultiplier tube

PL Photoluminescence

PLQY Photoluminescence quantum yield

QD Quantum dot

SHR Shockley-Read-Hall

TCSPC Time correlated single photon counting

VB Valance band

XRD X-ray powder diffraction

List of Figures

List of Tables

Contents

Chapter 1

Introduction

With the constant need for alternative energy sources and perpetual search for improved and more efficient optoelectronics and electronics in general, metal halide perovskites (MHP) have been extensively researched in the past decade for their rare and promising properties. Such properties include high absorption coefficient in the visible range of the electromagnetic spectrum, easily tunable bandgap, high photoluminescence quantum yield (PLQY), high defect tolerance and even self-healing properties. [21, 25]

The name perovskites refers to a family of crystalline materials of the form ABX_3 which were first discovered in the form of $CaTiO_3$ by a Prussian mineralogist Gustav Rose in 1839 and were (counter-intuitively) named after a Russian mineralogist Count Lev A. Perovskiy [25]. The perovskites studied nowadays for their photovoltaic and electronic applications are MHPs which have a very different composition, containing Pb, halides and organic molecules or Cs. However, their crystal structure remains the same. Perovkite crystal structure consists of two different cations, A^+

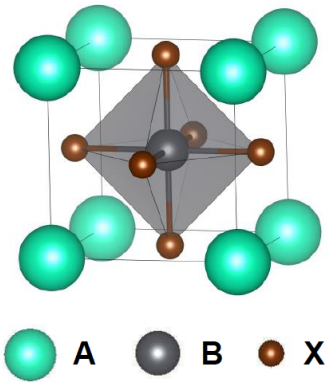

(a)

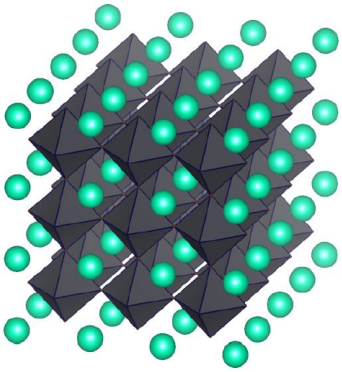

(b)

Figure 1.1: (a) Unit cell of a perovskite crystal (b) Perovskite lattice (Figure taken from [23]).

(for example Cs^+, methylammonium MA^+ or formamidinium FA^+) and B^{+2} (Pb^{+2}), and one anion, X^- (Cl^-, Br^- or I^-). Depending on the halide X chosen, one can tune the bandgap of the material covering the whole range of visible light. When an ideal cubic structure is assumed, the bivalent cation B^{+2} has a six-fold coordination and is surrounded by an octahedron of anions X^- as shown in Fig. 1.1 a). The larger monovalent cation A^+ then fills up the 12-coordinate vacancies formed by BX_3 units. A repeated array of perovskite unit cells results in a lattice structure shown in Fig. 1.1 b) [23]. Depending on the temperature of the environment, the phases of the crystal structure of MHPs' vary. In the case of $CsPbBr_3$ studied in this work, the stable phase of the crystal structure at low temperatures and up to 380 K is orthorhombic. This is also the lattice arrangement of the samples studied in this work. Above 380K and up to approximately 403 K, $CsPbBr_3$ has a tetragonal lattice while above 403 K the lattice transitions to a cubic phase. [32, 36] Apart from temperature induced changes to the lattice, quantum confinement and other nanoscale size effects can lead to various rotations or tilting of the lattice which in turn results in a change in the overlap of the electron wavefunctions implying different optical properties, for example the bandgap size [30, 38].

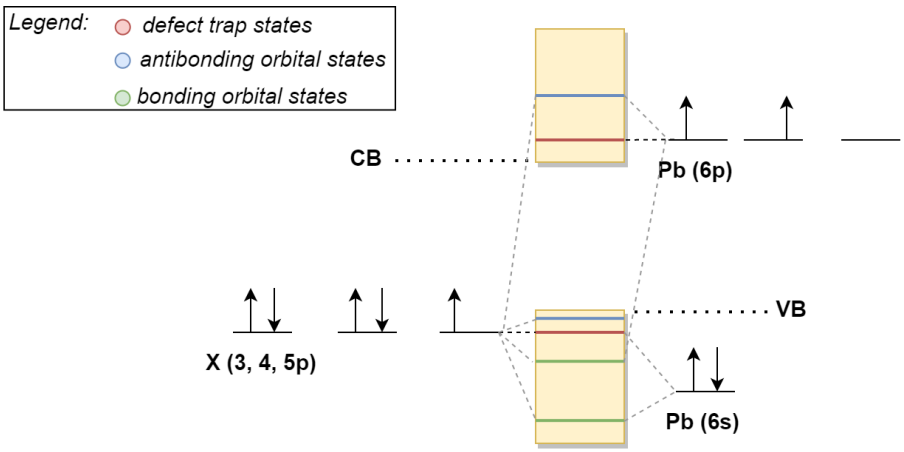

Figure 1.2: Electronic structure of a halide perovskite showing the bandgap formation where X is a halide (Adapted from [23]).

As previously mentioned, one of the peculiar properties of MHPs resulting from their crystal structure is their tolerance to defects which can be explained by an electronic structure diagram shown in Fig. 1.2. The edges of the conduction (CB) and valance bands (VB) are formed by antibonding orbitals; the halide p-orbital and Pb p- and s-orbitals, respectively [23]. The most common point defects create states that are contained within

the bands or near the band edges, however, theoretically never in the bandgap as in the case of traditional III-V semiconductors. The tolerance towards defects results in lower rate of non-radiative recombination which in turn results in a high PLQY which is one of the most crucial requirements for, for example, effective light emitting diodes (LEDs), lasers and photodetectors such as scintillation detectors.

Depending on the desired application of perovskites, one has to tune their chemical composition. And as the character of the perovskite crystal structure is very flexible, there is a large pallet of different element combinations to choose from. For example, solar cells and LEDs show higher efficiencies with organic halide perovskites, containing MA^+ and FA^+ ions. While one of the most promising lead halide perovskites for scintillating applications in photodetectors is an all-inorganic $CsPbBr_3$ halide perovskite which is also the focus of this work. Compared with traditional scintillators, such as organic and oxide scintillators, $CsPbBr_3$ could offer low-cost production as it is easily produced at low temperatures via solution processing as well as low detection limit for radiation and higher resolution via the employment of nanostructures.

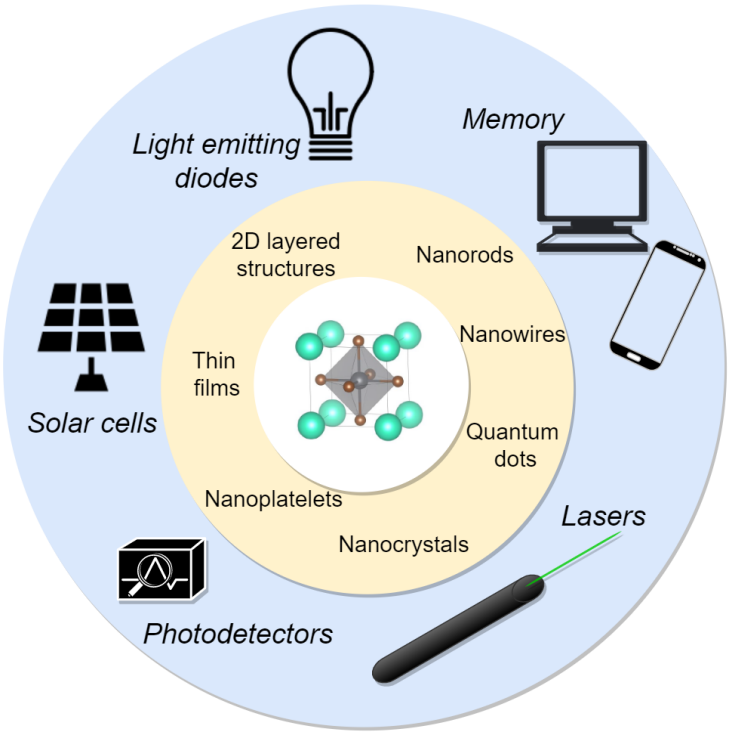

Figure 1.3: The large pallet of element combinations forming perovskites leads to a great variety of applications including solar cells, LEDs, photodetectors and more.

In recent years, the applications of 3-dimensional (3D) $CsPbBr_3$ across 2-dimensional (2D) polycrystalline thin films and up to 0-dimensional (0D) nanocrystals for photodetectors have been studied. Note that the dimensionality mentioned refers to the number of dimensions in which a particular structure exceeds the nanoscale. Additionally, even quantum confined $CsPbBr_3$ in the form of a multilayered 2D system (now referring to the number of dimensions in which charge carriers can travel freely) has been explored and demonstrated a strong sensitivity towards polarization of light which is of merit in the fields of communication and security [37].

A number of interesting and advantageous properties has also been observed for 0D and 1D nanoscale perovkites. Higher dimensional polycrystalline thin films, in general, consist of a number of grains which can cause degradation of the material as a high tendency of charge recombination at such sites is observed [21]. Furthermore, perovskite polycrystalline thin films exhibit high mobile ionic defects which negatively affect their optical and electronic properties, e.g cause hysteresis in I-V characteristics as the defects can easily migrate under an applied bias. On the other hand, low dimensional perovskites demonstrate superior properties due to quantum confinement effects and higher crystallinity. As a result, perovskite quantum dots (QD), nanocrystals, nanorods and nanowires (NWs) possess wider bandgap with the possibility of effortless tunability and above all a higher PLQY. The increase in PLQY compared to higher dimensional perovkites is unexpected as low dimensional structures have higher surface to volume ratio which implies a higher probability of surface defect related non-radiative recombination to occur. Moreover, low dimensional perovskite structures prove to have fewer ionic defects as well as grain boundaries which consequently implies improved charge carrier mobility. However, charge carrier transport properties still remain favourable in thin film perovskites as charges in low dimensional perovskites have to overcome many potential barriers as they travel.
[21, 22]

Among properties of such a high merit in optoelectronic and electronic fields, even low dimensional perovskites suffer from poor intrinsic stability caused by the nature of their crystal structure and poor extrinsic stability under external environmental conditions such as humidity, air, high temperature and electromagnetic radiation. Perovskite long-term

instability has been tackled by two main approaches so far; chemical and physical protection approach [21, 25]. While the chemical approach naturally focuses on understanding and manipulating the chemical processes underlying the decomposition of perovskites [26, 27], the idea behind the physical approach is to give an additional physical protection to the perovskite by the means of, for example, encapsulation or the application of a photocurable polymer layer on the top of the perovkite's surface [35, 39]. One such a physical protection approach is the growth of perovskite nanowires in porous templates such as anodized aluminium oxide (AAO) [17, 35, 38]. The AAO template not only provides increased physical and mechanical stability of the embedded soft perovskite but also a fine control over the nanowires' dimensions and their crystal structure.

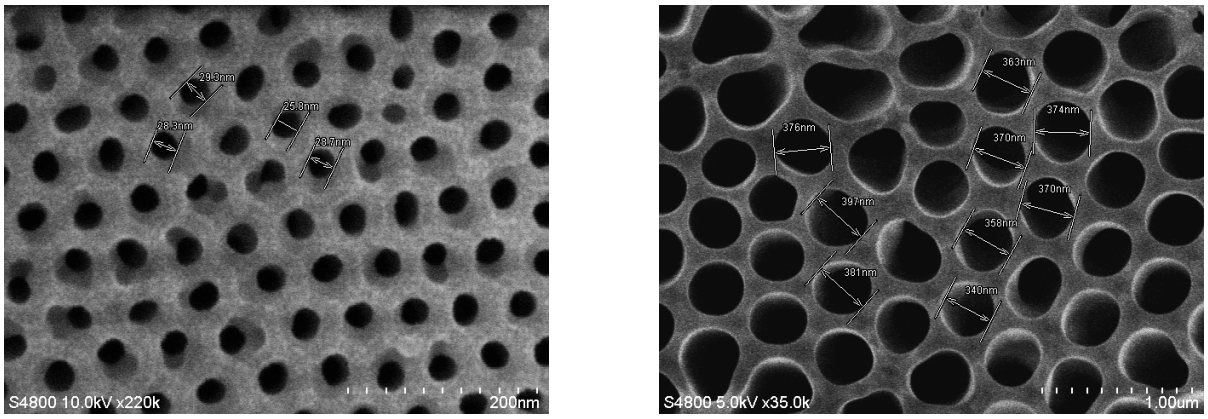

(a) (b)

Figure 1.4: An example of AAO template used for growing (a) 30 nm diameter (b) 360 nm diameter nanowires where the diameters of some of the pores are indicated (Credits to Zhaojun Zhang).

In this work, samples of $CsPbBr_3$ NWs grown in AAO template with varying NW diameter from 30 to 360 nm (D30-D360), defined by the AAO pore size, are optically characterised using steady-state and time-resolved photoluminescence measurement techniques. Such characterisation is done with the aim of understanding the photophysical processes taking place in such a material and identifying the most suitable NW diameter for a future X-ray scintillating detector application. Examples of scanning electron microscope (SEM, see Appendix A for more information) images of two of the AAO templates used in the experiments for the purpose of this thesis are shown in Fig. 1.4 for a better picture.

Chapter 2

Scientific Background

2.1 Scintillation Detectors for X-rays

The main components of a scintillation detector are a scintillation material, an optical detection system and data acquisition electronics. The scintillation material converts an X-ray into a visible light photon which is detected by an optical detection system. Here the photon is transformed into an electric signal which is collected, analysed and digitised by the data acquisition system. The detection system can be based on a variety of different technologies, for example, complementary metal–oxide–semiconductor (CMOS) technology, thin film transistors (TFTs) or on a simpler photomultiplier tube (PMT) or a photodiode [10]. A general schematic of the working principle of the detector is illustrated in Fig. 2.2. The further discussion in this section will focus on the physics of the scintillation itself, however, one can find more information on the different types of optical detection systems and data acquisition in [8, 10, 12].

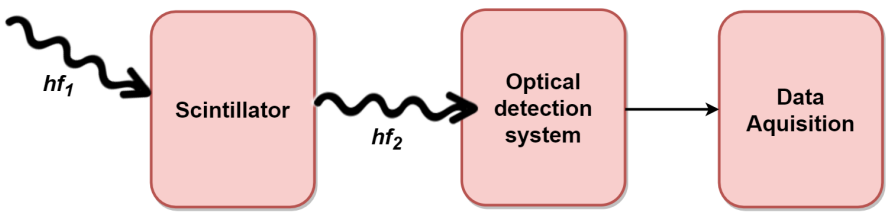

Figure 2.1: A general path of a scintillation detector system.

When a high energy X-ray photon with energy hf_1 impacts the scintillator, the photoelectric effect, Compton scattering and pair production occur resulting in many electron-hole (e-h) pairs generated in the scintillator. The contribution of each of the three processes depends on the X-ray energy hf_1. If a low energy X-ray (below 100 keV) strikes the scintillator, photoelectric absorption is the dominant effect. In this case, photoelectrons are generated upon the photon absorption which subsequently excite atomic electrons from the VB to the CB via impact ionisation giving rise to e-h pairs. On the other hand, Compton scattering is favoured for medium range energies around 1 MeV as only part of the photon energy can contribute to the e-h pair generation. At energies above 1 MeV, pair production has the highest cross-section. In general, the average amount of e-h pairs generated is around 1000 per event, however, it is strongly dependent on the ionisation energy hf_1. It should be noted that photoelectric absorption is usually assumed to be the main source of e-h pairs as the cross-sections of Compton scattering and pair production are very low for the usual X-ray energies used in research and most of the applications.

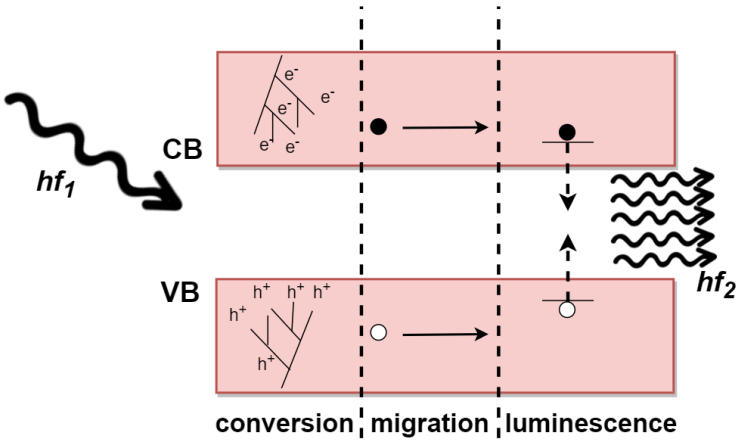

Figure 2.2: An overview of scintillation and its three main sub-processes.

After e-h pairs are generated, the electrons and holes migrate through the CB and the VB, respectively, until reaching a luminescence centre. Here, both the electrons and holes are trapped and their recombination leads to emission of a photon with energy hf_2 where $hf_2 < hf_1$. Depending on the ionisation energy hf_1 of the X-rays, the scintillator emits a particular number of photons which generate an electric signal of a certain magnitude. Thus one has a direct link between the amount of radiation detected and an electronic signal. [8, 12, 31]

An example of how one can compare the performance of a scintillating material is shown in Fig. 2.3. The scintillation data was obtained from a different batch of the same kind of samples as those studied in this work. The plot of the emitted scintillation intensity versus emission wavelength shows that the intensity of the visible light photons emitted by the scintillating $CsPbBr_3$ (hf_2 from the previous discussion) is higher for samples with smaller NW diameter. In the end of this thesis, we will hopefully be able to confirm or challenge this result for the new batch of the samples studied here.

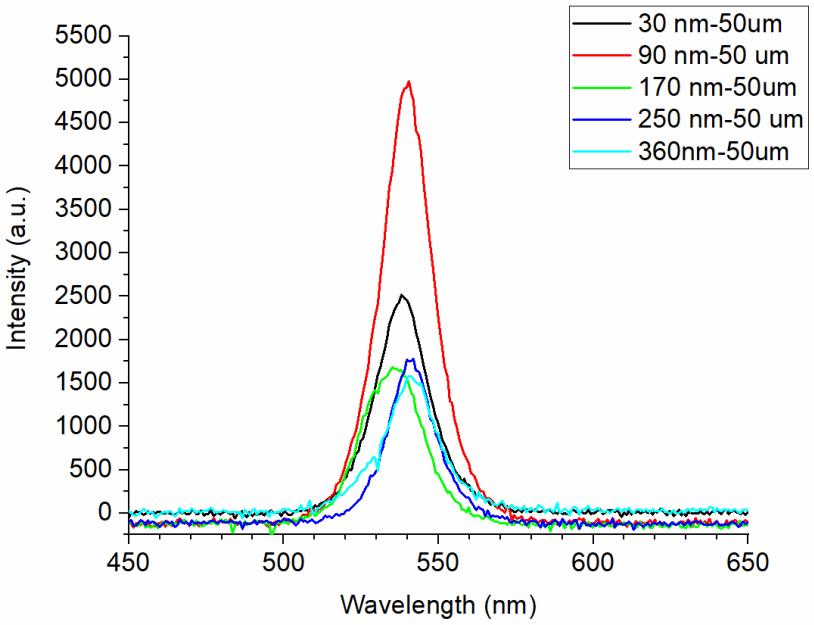

Figure 2.3: Results of the first scintillation test of a different batch of the same samples done by Zhaojun Zhang.

2.1.1 Key Parameters

Based on the physics of scintillation, one can define key characteristics of an ideal scintillator. One of the most crucial variables is the *response-decay time* defined as the time taken to convert an X-ray photon into visible light photons. The response-decay time is mainly affected by the migration and luminescence sub-processes of scintillation as conversion of X-ray into an optical excitation occurs almost instantaneously. The response time of a material is characterised by the time taken for the migration to occur. While the decay is determined by the time taken for the excited carriers to recombine and give off luminescence. The decay time can be extracted from a single exponential decay of the luminescence intensity which is also the simplest description of a decay. The mathematical expression for such a decay is,

$$I(t) = I_0 e^{\frac{-t}{\tau}}, \tag{2.1}$$

where I_0 is the initial intensity and τ describes the material's decay kinetics.
It is important to note that luminescence decays are not always described by a single exponential and can involve more complicated multi-exponential description, where samples demonstrate multiple decay times due to local quenching, non uniform composition or multiple recombination processes involved [7]. In such decay kinetics, a charge carrier concentration dependence of the decay time is observed. For an ideal scintillator, a decay time as short as possible is desired.

A second fundamental property of a scintillator is the *conversion efficiency* η defined as,

$$\eta = E_{vis} \cdot \frac{S \cdot Q}{\beta \cdot E_g} = E_{vis} \cdot \frac{N_{ph}}{E}, \tag{2.2}$$

where E_{vis} is the energy of generated visible light photons, E_g is the bandgap of the scintillator, β is a constant, S and Q are the quantum efficiencies of the transport and luminescence sub-processes and E is the energy of the interacting X-ray photon and N_{ph} is the number of visible photons produced by an X-ray of a certain energy E.
The variable N_{ph} is directly connected to another parameter; the *light yield* of a scintillator. The light yield quantifies the actual number of photons detected by the electronics. Due to unavoidable dead times of photodetectors, however, the light yield never exceeds the value of N_{ph}.

For as many X-ray photons to be detected by the scintillator, a high stopping power, i.e. the ability to block, is required. If only photoelectric absorption is considered as the main e-h pair generator, the stopping power is directly proportional to the material density and effective atomic number Z_{eff}, $\sim \rho Z_{eff}$. Therefore denser materials such as $CsPbBr_3$ are selected for X-ray detection. [8, 31]

2.2 Electronic Transitions in Semiconductors

Upon the excitation of a semiconductor by the means of, e.g X-rays or visible light photons of energy $E > E_g$, the electrons are excited from the VB to the CB giving rise to photogenerated charge carriers. Depending on the nature of the material's structure and dimensionality, one can distinguish between two limiting types of generated photocarriers; free carriers and electrostatically bound e-h pairs referred to as excitons. In the case of traditional inorganic bulk semiconductors, such as III-V semiconductors, the majority of the photocarriers are free charge carriers. This is a consequence of very low exciton binding energies ranging from 0.6 - 6 meV at room temperature for typical III-V semiconductors such as GaAs, InSb, InAs and InP [2, 4, 18]. These binding energies are significantly lower than the thermal energy of the semiconductor system k_BT ($\sim$ 25 meV) therefore the existence of excitons under room temperature conditions is inconceivable. For any observations of excitons in this type of semiconductors, one would have to cool down the material to temperatures as low as tens of Kelvins [29].

After photogeneration, free carriers thermalize at the band edges and undergo three main recombination processes; radiative bimolecular, nonradiative Auger and Shockley–Read–Hall recombinations as visualised in Fig. 2.4 a). In bimolecular recombination, Fig. 2.4 a) 2), a photon of the energy E_g is emitted as a consequence of annihilation of an electron and a hole. Alternatively excited carriers can recombine nonradiatevily via Auger recombination Fig. 2.4 a) 3), where the energy released from the recombination is transferred to a third carrier, or via Shockley–Read–Hall (SHR), Fig. 2.4 a) 4) trap-mediated recombination. [6, 29]

On the other hand, organic semiconductors as well as inorganic semiconductor 0D structures such as QDs exhibit excitonic nature of the photogenerated carriers which results in highly preferred radiative recombination. Moreover, as the size of a bulk 3D inorganic semiconductor is decreased in all three dimensions and QD is realised, quantum confinement effects impact the bandgap energy. The bandgap energy in such a system is then larger than in a bulk form, as depicted in Fig. 2.4 a), and increases with decreasing size of the QD as $\frac{1}{r^2}$ [11]. The effects of quantum confinement on the bandgap can only occur if one of the materials dimensions is smaller than the Bohr-excition radius of the particular material, in the case of $CsPbBr_3 \approx 7.5$ nm [20]. Thus for structures well above the quantum confinement regime, as it is the case for all NW samples studied in this work, no change in emission wavelength is anticipated by quantum mechanics.

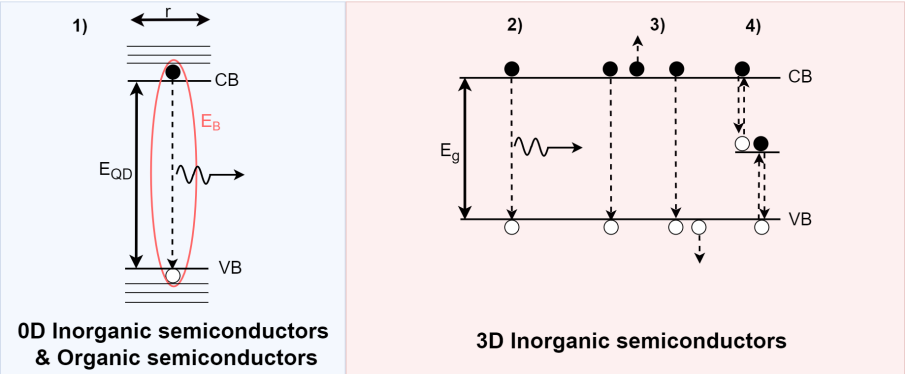

(a)

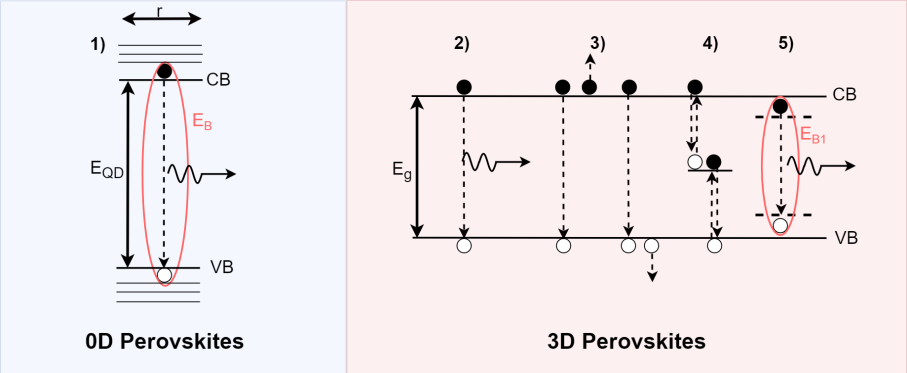

(b)

Figure 2.4: A comparison of the transitions in (a) 0D and 3D III-V semiconductors and (b) 0D and 3D perovskites where the recombination processes shown are 1) radiative bound exciton, 2) bimolecular radiative, 3) Auger, 4) SHR recombinations and 5) radiative bound exciton recombination in bulk.

In the case perovskites, it has been suggested that their carriers are a mixture of the two limiting cases, i.e. free charge carries and excitons coexist, and radiative excitonic recombination can occur in all dimensions as shown in Fig. 2.4 b). Such photophysical effects are a consequence of high E_B, greater than k_BT [28, 29]. The balance between the two types of carriers can be calculated by a well-known Sara-Langmuir equation,

$$\frac{\phi_{fc}^2}{1-\phi_{fc}} = \frac{1}{n}\left(\frac{2\pi\mu k_B T}{h^2}\right)^{\frac{3}{2}} e^{\frac{-E_B}{k_B T}}, \tag{2.3}$$

where n_{fc} and n_{exc} are the free charge carrier and exciton densities respectively, n is the total excitation density (n=n_{fc}+n_{exc}), ϕ_{fc} is the fraction of free charges over the total excitation density ($\phi_{fc} = \frac{n_{fc}}{n}$), μ is the reduced exciton mass, T is the temperature, E_B is the exciton binding energy, h is the Planck's constant and k_B is the Boltzmann's constant. [1, 14, 29]

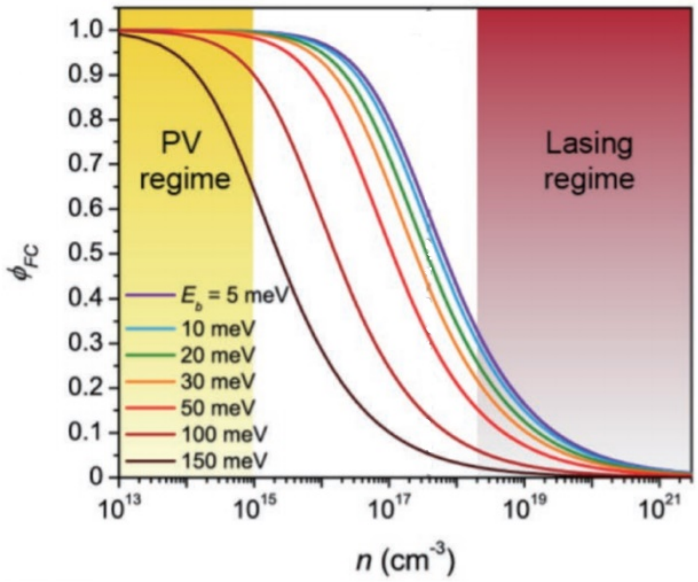

Figure 2.5: Visualisation of Saha's equation at room temperature conditions with photovoltaics (PV) and lasing regimes highlighted where the reduced exciton mass used is 0.1 m_e. (Figure taken from [29]).

The expression is visualised in Fig. 2.5 where the fraction of the free charge carriers ϕ_{fc} is plotted as a function of the total excitation density of carriers n for different exciton binding energies E_B. The preferred regimes for different applications, such the for photovoltaics (PV) and lasers are also included in the figure. While the working regime of photodetectors, not highlighted in the figure, spans a large range between $\sim 10^4$ cm^{-3}

to $\sim 10^{15}$ cm^{-3} [33]. As the reported, exciton binding energy is around 40 meV for low dimensional $CsPbBr_3$ and the total excited charge carrier density in our experiments is $\sim 10^{16}$cm^{-3}, we can assume that around 90% of the photoexcited carriers in our samples are free charge carriers [29, 33].

While photovoltaic applications favour semiconductors with low E_B ($E_B < k_BT$) where the photogenerated excitons dissociate spontaneously within a couple of picoseconds and give rise to free charge carriers, photodetectors and LED's require quite the opposite for their optimal functionality. As a result of high E_B, the excitons stay bound for longer periods of time and in the end recombine radiatively thus giving high PLQY. Even though the nature of the dominant photogenerated carriers in MHPs is uncertain, demonstrated by the wide range of E_B obtained so far, it has been shown that low dimensional MHPs show superior properties, namely an increased PLQY. Such an enhancement is the aftermath of quantum and dielectric confinements where due to the increased E_B, radiative recombination is preferred [29].

2.3 Photoluminescence

Having discussed the working principles of scintillating materials and their possible electronic transitions, we will now turn to the technique and the phenomenon which can help us optically characterise such materials. This phenomenon is photoluminescence (PL). In general, PL describes an emission of light from a substance where photos are the source of excitation energy.

PL consists of multiple physical processes which can be collectively described by a band diagram in Fig. 2.6. The initial step of photoluminscence is the absorption of a photon which leads to an excitation of the material's electrons from a state in the VB to a state in the CB. Before emission occurs, the excited electrons and holes rapidly and nonradiatively relax to the lowest excited state via thermalisation. From the diagram, one can notice that the energy of the emitted photons is lower than the energy absorbed by the material. This effect was first described by Sir George Stokes in 1852 and in his honour the effect is now named *Stokes shift*. The red shift in emission is caused by thermal

relaxation to the lowest exited state and as well as due to internal effects of the material (e.g. energy transfer). A second universal theorem of PL is *Kasha's rule* which states that the emission spectra are generally independent of the excitation wavelength. [7, 11]

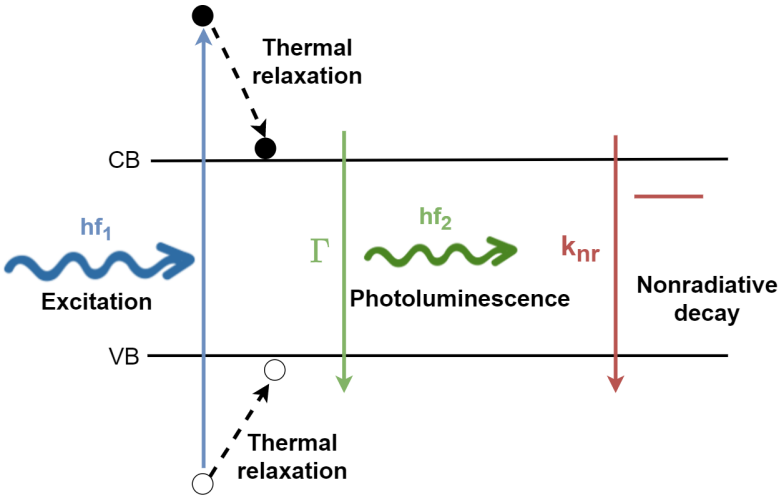

Figure 2.6: Photoluminescence and the two main subgroups of decay mechanisms; radiative and nonradiative.

Even though the initial interaction of a scintillating material with X-rays is different than the one with a lower energy photon as outlined above, the final desired outcome of the X-ray excitation process in a scintillator is a photon which is emitted as immediately as possible. If therefore one wants to study the decay time of the excited charge carriers in a scintillating material, a traditional PL spectroscopy using a laser for the excitation can be used.

As mentioned, a key property of photoluminescent materials which can unravel the nature of photogenerated carriers as well as possible carrier recombination processes is the decay τ which is defined as the average amount of time a material remains in an excited state after excitation. The decay of an excited carrier population in its simplest form can be described by a single exponential decay curve of the PL intensity as per Eq. (2.1). However, such description is not appropriate for the case of our MHP samples. In our case, the decay can be approximated by the following multi-exponential function,

$$I(t) = \alpha_1 e^{\frac{-t}{\tau_1}} + \alpha_2 e^{\frac{-t}{\tau_2}} + +\alpha_3 e^{\frac{-t}{\tau_3}}, \tag{2.4}$$

where α_1, α_2 and α_3 are the decay amplitudes which give the weight of each decay time, and τ_1 and τ_2 are the material's decays. The average decay time, $\langle\tau\rangle$ is then computed by performing a weighted average as,

$$\langle\tau\rangle = \frac{\alpha_1\tau_1 + \alpha_2\tau_2 + \alpha_3\tau_3}{\alpha_1 + \alpha_2 + \alpha_3}. \tag{2.5}$$

Chapter 3

Method

3.1 Sample Preparation

$CsPbBr_3$ nanowires were grown in a 50 μm thin anodized aluminium oxide (AAO) templates with an opening on both ends from Shenzhen Topmembranes Technology Co., Ltd. The diameter of the nanowires was determined by the pore size; ranging from 30 to 360 nm (D30-D360).

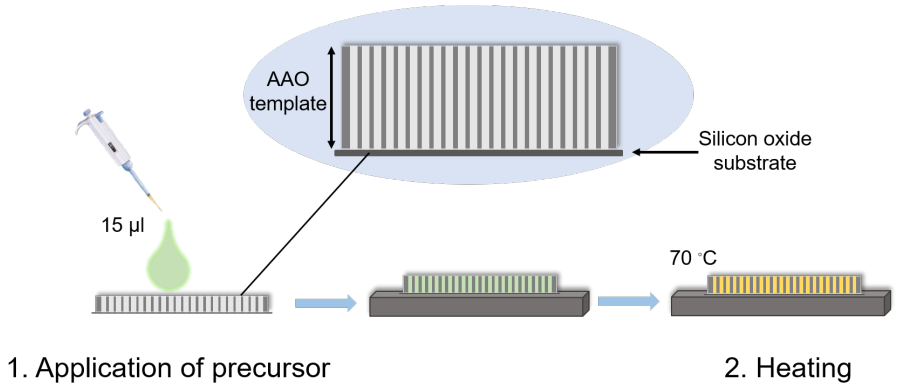

Figure 3.1: The main steps in the sample preparation procedure.

Before introducing the precursor to the templates, the templates were treated with 1 minute oxygen plasma to improve the surface quality and thus ensuring smooth filling of the pores with the precursor. The precursor used in this case was dimethylsulfoxide (DMSO) containing dissolved CsBr and $PbBr_2$ compounds. The optimal concentration of the precursor used was 0.45 M which is also the maximum concentration at which CsBr and $PbBr_2$ compounds are still solvable in DMSO. 15 μl of the precursor was injected

on a silicon oxide substrate which followed by the application of the AAO template. The precursor then infiltrated the pores of the template driven by the action of capillary forces. In the second step, the sample was placed on a hot plate, heated to 70°C, for 30-45 minutes. As a result, radiation and air stable $CsPbBr_3$ samples were obtained. Examples of cross-section images of D30 nad D360 samples taken with SEM by Zhaojun Zhang are displayed in Fig. 3.2.

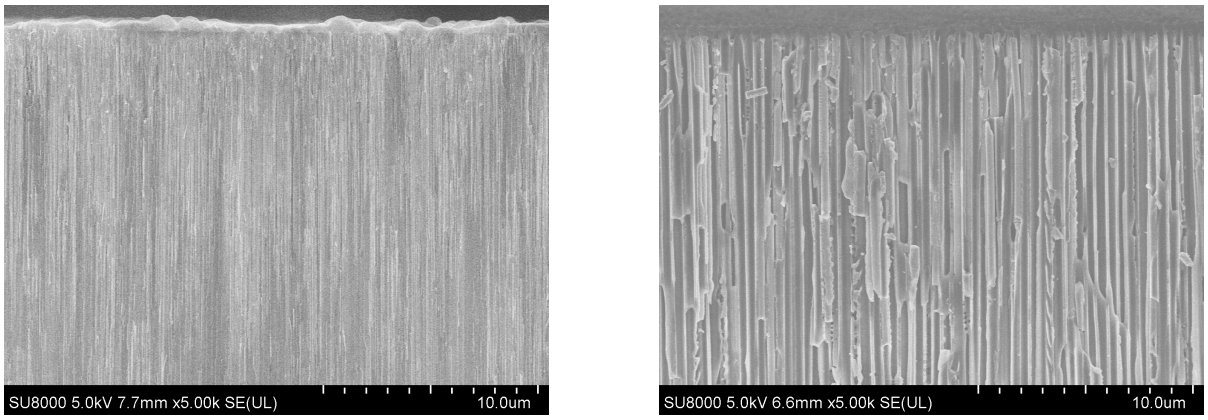

(a) (b)

Figure 3.2: Images taken with SEM of (a) 30 nm and (b) 360 nm diameter samples made by Zhaojun Zhang.

3.2 Steady-state Photoluminescence

Set-up

The spectral measurements of the samples were obtained with PL steady-state technique. The key component of PL spectroscopy setup is a epi-fluorescence microscope. As illustrated in Fig. 3.3, the main function of the microscope is the illumination of a sample with a selected range of wavelengths or a specific wavelength and subsequent separation of the excitation light from much fainter PL. Such a functionality is possible due to the presence of an optical block; consisting of an excitation clean-up filter, dichroic mirror and an emission long pass (LP) filter, referred to collectively as a cube. An epi-fluorescence microscope usually has a number of such cubes which are suitable for different experimental needs (different excitation and emission wavelengths etc.) and which one can switch between. The clean-up filter selects a band of excitation wavelengths or a single wavelength of the incoming light from the light source, laser in our case. The dichroic

mirror then reflects the selected excitation light towards the sample which is subsequently excited and gives of PL.

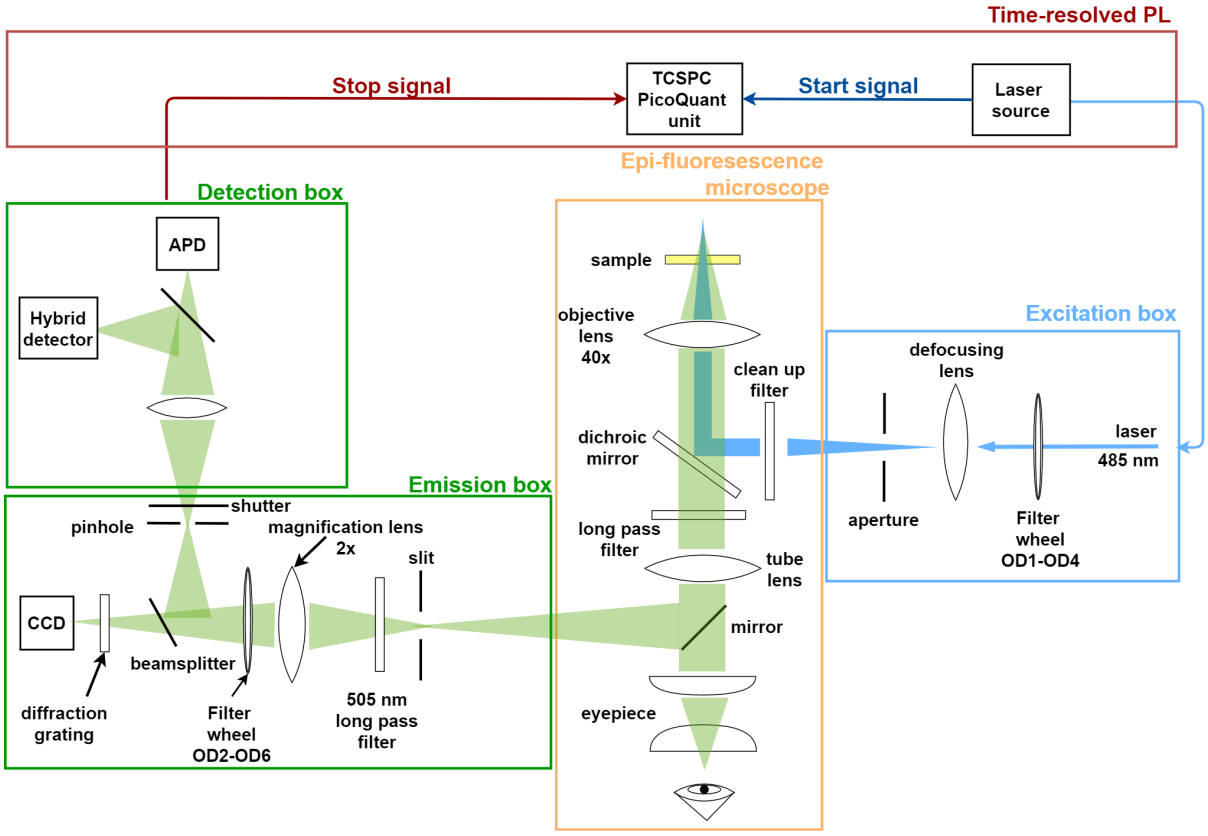

Figure 3.3: A schematic of the optics setup used for the PL steady-state (From Excitation box up to Emission box) and the time-resolved measurements (From Excitation box up to TCSPC unit).

The emitted light then passes through the dichroic mirror while the laser is reflected back towards the incoming path. To ensure that the laser does not reach the selected detector, a LP emission filter, which only allows light above a certain wavelength to pass through, is put in place. The parameters of the particular cube used during our experiments can be found in Appendix B.

The fully electronically controlled optical set-up, shown in Fig. 3.3, was used for both steady-state and time-resolved measurements. One can divide the set-up into four parts correlated to the main steps in the PL spectroscopy technique; excitation box, the epi-fluorescence microscope itself, emission box and detection box (solely used for time-resolved PL). Before the light emitted from a laser source reaches the microscope, it passes through one of the four neutral optical density filers attached on a filter wheel located in

the excitation box which allows for a control over the amount of excitation power density reaching the sample. Optical density (OD), also referred to as absorbance, is defined as a measure of transmittance through an optical medium, with the following mathematical definition

$$OD = -log_{10}\frac{I_0}{I}, \tag{3.1}$$

where I_0 is the intensity of the incident light on the medium and I is the intensity of the transmitted light [7]. To establish some intuition, OD3 filter attenuates the optical power density of the light source by a factor of 1000 while OD2 filter by a factor of 100.

The laser then travels through a defocusing lens and aperture both of which control the size of the excitation spot on the sample. Continuing through the setup, the laser passes through the microscope, excites the sample and PL is emitted. To view the PL, one can choose to view the PL directly with the eyepiece or on a computer screen utilising a charge-coupled device (CCD) by switching a mirror in the microscope. When the CCD is selected for the PL detection, the PL enters the emission box and passes through a slit, additional 505 nm LP filter to avoid laser leakage (due to an imperfect transmission profile of the LP filter in the microscope's cube), a 2x magnification lens and a emission filter wheel (containing OD2, OD3, OD4 and OD6 filters) before reaching the CCD. The objective and magnification lenses give a total magnification of 80 while the CCD has resolution of 1.6 μm limited to its chip size. Thus the sample features which can still be resolved in a PL image are limited spatially to 0.2 μm range. To switch from a microscopic to a spectral measurement regime, one simply electronically inserts the diffraction grating in front of the CCD and limits the PL detected by closing the metal slit to allow for diffraction of the PL as shown in Fig. 3.4.

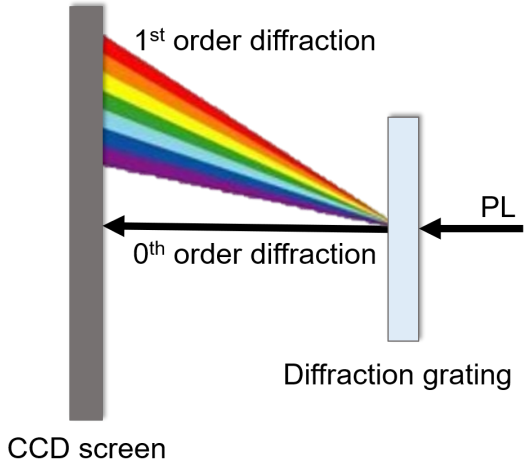

Figure 3.4: A schematics of the diffraction occuring when a diffraction grating is inserted into the PLs path.

Experimental Procedure

As the previously reported PL emission of $CsPbBr_3$ was around 520 nm [30, 36, 38] therefore the excitation light chosen in this case was a 485 nm pulsed diode laser with repetition rate range 100 Hz - 80 MHz, a 150 - 200 ps pulse duration and power up to 3.6 mW. The emission spectra of all samples from both top and cross-section were systematically obtained. It is worth noting that during the cross-section readings the sample had to be attentively placed on a homemade aluminium-glass sample holder. The two geometries are illustrated in Fig. 3.5. For every measurement, a PL image of the selected sample area and an image of the diffraction patter (PL spectrum) was recorded. Where needed, a bright field transmission image of the sample was recorded. The obtained data was then analysed with image processing program Image J and python script attached in Appendix E. All peaks were fitted with Gaussian curves.

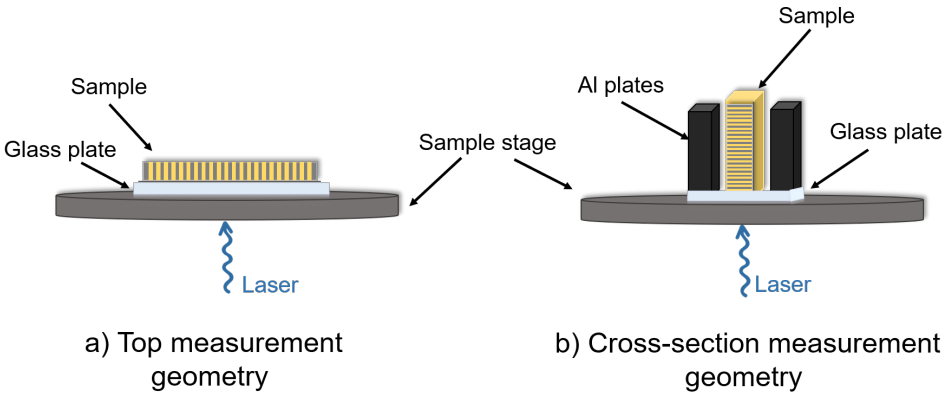

Figure 3.5: The two measurement geometries set up for both steady-state and time-resolved PL.

Additionally, neutral OD filters on excitation and emission filter wheels were used to adjust the excitation or emission power densities of the laser and emitted PL. The adjustments of excitation and emission filters were done mainly to prevent the damage of the detector and to undertake power dependent measurements. When measuring the power dependence of excitation light on the emission wavelength, the OD of the excitation filter was decreased from OD4 to OD1 and emission filter was adapted in order to prevent the detector from oversaturating. Lastly, it is important to note that all measurements were repeated to ensure that a general instability nature of perovskites did not affect the results.

3.3 Time-resolved Photoluminescence

Set-up

The time-resolved PL measurements were done using time correlated single photon counting (TCSPC) technique. The same set-up as for steady-state PL measurement was used with the addition of a TCSPC PicoQuant hardware and the beam splitter switched to the position in front of the CCD detector and thus letting 50 % of the emitted PL pass towards the avalanche photodiode (APD) / hybrid detector and 50 % transmit to the CCD. The hybrid detector used in this set-up was a PicoQuant PMA hybrid detector and the APD was a PDM series photon counting detector. The response time of the hybrid detector was under 130 ps while for the APD it was less than 50 ps.

TCSPC is a highly sensitive technique which allows for the measurement of the decay of the excited charge carrier population in the sample material. The high sensitivity is achieved by the detection of a single photon per an exiting laser pulse. In a typical TCSPC measurement, the sample is excited with a pulsed laser, here a 485 nm pulsed diode laser with a repetition rate range 100 Hz - 80MHz, a 150 - 200 ps pulse duration and power up to 3.6 mW was used (same laser as for the steady-state PL measurement).

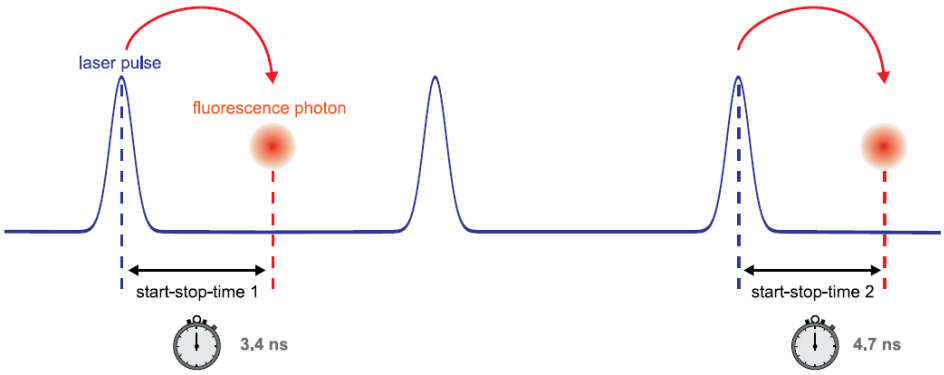

Figure 3.6: An illustration of the start-stop mechanism in TCSPC (Figure taken from [15]).

When the laser is switched on, it gives a start signal to the TCSPC unit, blue pulse in Fig. 3.6. The laser pulse then travels towards the sample passing a shutter and a motorised excitation filter wheel. Upon the laser arrival, excited sample emits PL photons which propagate towards the APD or a hybrid detector via a motorised emission filter and a beam splitter. Once a PL photon is detected by the APD/hybrid detector, a stop signal,

red photon in Fig. 3.6, is passed to the TCSPC unit and the rest of the photons coming from the same excitation pulse is not detected. The detected event (start-stop) is stored in a specific channel of the electronics of the TCSPC unit depending on the delay time as shown in Fig. 3.7. This process is repeated over a selected amount of accumulation time until a histogram of detected photons in different channels is obtained. [15, 16]

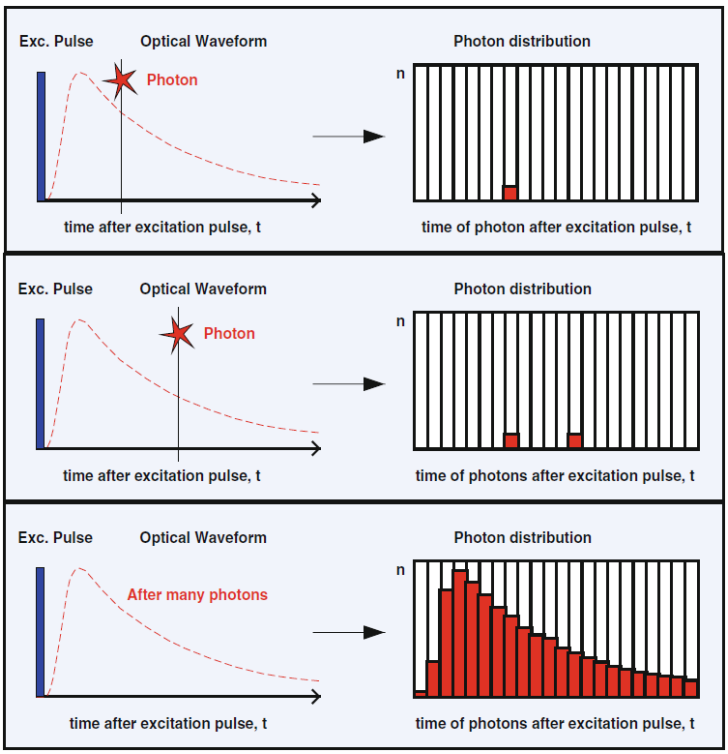

Figure 3.7: Evolution of the photon counts leading to a histogram of accumulated photon signals (Figure taken from [16]).

Experimental Procedure

Decay measurements of each sample from the top and cross-section of the sample were measured either with the APD or the hybrid detector, depending on the aim of the experiment. In case of measuring the decay from a specific sample spot, the APD was used due to its smaller detection area where the most sensitive area could be correlated to a single pixel coordinate on the CCD. Any direction from this coordinate the sensitivity dropped within 7 pixels by a factor of 10^3 , however the APD was still able to detect any signal hitting its detection area with 1 μm radius. When an average decay of the whole illuminated sample area was the main interest, a hybrid detector with a detection area radius 3 mm was used.

For the power dependent decay measurements, the excitation and emission filters were used in an manner identical to the spectral measurements. Both measurements from the top of the sample and the cross-section entailed a PL image of the selected sample area and a decay curve obtained with PicoQuant software which had to be analysed and plotted using a python script attached in Appendix E. Since the instrument response function of the set-up at the excitation frequencies used was insignificant with respect to the decay times measured ($\sim$ 200 ps), a usual deconvolution procedure of the obtained decay curves could be skipped. The decay curves were thus fitted with Eq. (2.4) with a previously mentioned python script.

3.4 Calibration of the Set-up

In order to understand the PL spectra obtained, one had to first proceed with a calibration of the CCD camera for the conversion between pixels and nanometers to be possible. For this purpose, light from an ordinary fluorescent tube lamp was used. The spectrum of the fluorescent lamp from the lab can be seen in Fig. 3.8 a). In order to obtain as large detection range as possible, a cube with a 405 nm LP filter, lowest filter available in the lab, was used. Knowing the main emission lines of mercury, europium and terbium in the visible light range and measuring the centre peak values in pixels using an image processing program ImageJ, one could obtain the conversion factor for this set-up. This was done by simply plotting the emission wavelength of the prominent peaks (See Appendix D) found from literature [41] versus the peak centre values in pixels and subsequently fitting the data with a linear regression method. The factor was obtained to be

$$\Delta\lambda/\Delta p = 2.0848 \pm 0.0103 \quad \text{nm/pixel}.$$

A rounded value of 2.085 was then used for the conversion between pixels and nanometers in the data analysis of the PL spectral data. This value also determined the spectral resolution of the set-up.

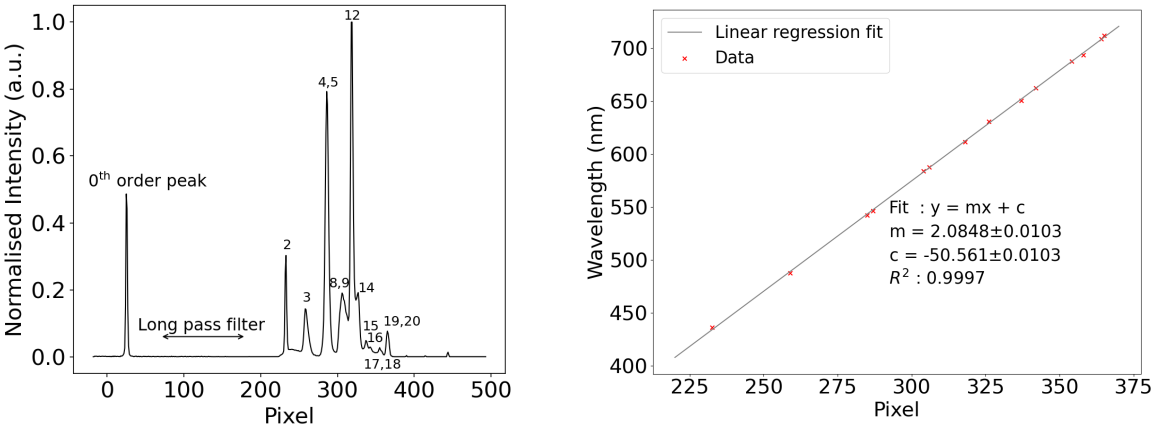

(a) (b)

Figure 3.8: (a) The spectrum of the fluorescent lamp used for calibration, where the identified peaks are numbered according to [41] (See Appendix D to identify each peak). (b) Fitting of the data obtained from the spectrum.

Chapter 4

Results and Discussion

4.1 PL Emission Spectra

4.1.1 Dependence of Emission Wavelength on Pore Diameter

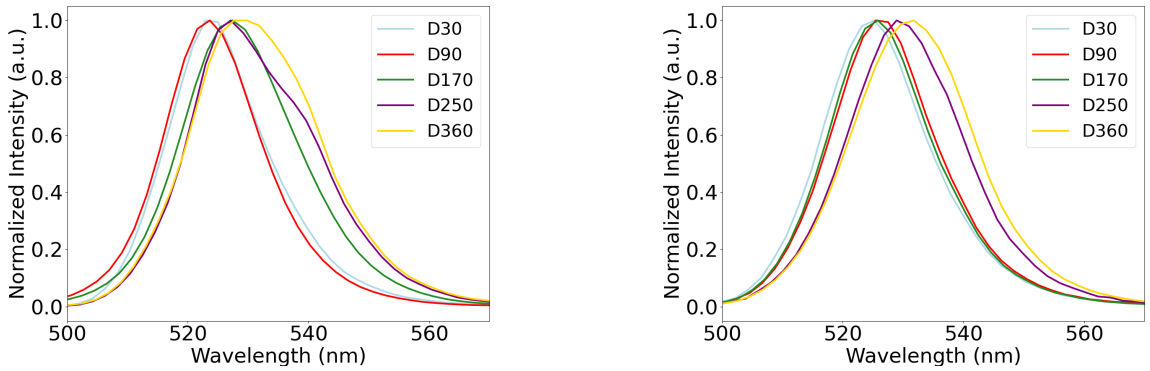

Figure 4.1: The emission spectra of samples with diameter ranging from 30 to 360 nm measured with 1.4 W/cm^2 excitation power density and 80 MHz repetition rate from the (a) top and (b) cross-section .

As previously reported among others by Oksenberg et al. [30] and Zhang et al. [38], one generally observes a blue-shift in emission wavelength as $CsPbBr_3$ NW structures advance towards a smaller diameter. An analogous trend has been observed here with the emission wavelength varying between 524 - 532 nm when increasing the size of the diameter from 30 to 360 nm as shown in Fig. 4.1. The exact values, including the full width at half maximum (FWHM), obtained in first approximation by Gaussian peak fitting of the spectra can be found in Table 4.1. When looking at the recorded spectral

peaks in Fig. 4.1, one can notice the only tenths of nanometers difference between samples with 30-170 nm diameter, where the emission from the top even suggests the D90 sample to have the most energetic emission. Such minuscule emission shifts are observed from both the top and the cross-section of the sample. One of the possible reasons could be the in-homogeneity of the samples and poor crystal quality as emission wavelengths obtained generally showed variation when looking at different parts of the sample. This argument can be further supported by visible size and shape diameter variations within the samples and a general quality variation observed with SEM by my colleague Zhaojun Zhang, shown in Fig.1.4 in the *Introduction chapter*. Moreover, a broadening of the emission peaks with increasing diameter was observed for both geometries measured, hinting possibly a more regular structure of the smaller diameter wires.

Table 4.1: Summary of the exact central wavelengths and peak FWHM obtained from the cross section(λ_{cr} and $FWHM_{cr}$) and top (λ_{top} $FWHM_{top}$) of the samples.

Sample D [nm]	λ_{cr}[nm]	$FWHM_{cr}$ [nm]	λ_{top}[nm]	$FWHM_{top}$ [nm]
30	524.5	21.8	524.9	20.3
90	526.3	23.0	524.1	20.3
170	526.6	23.1	528.5	23.6
250	531.1	25.2	530.4	25.2
360	531.6	24.6	531.1	25.2

Looking at the PL spectra in 4.1 in more detail, one can notice the appearance of a red-shifted shoulder of the larger diameter peaks, D250 and D360 samples, which is more apparent for the PL measurements performed from the top of the samples. Such a red-shifted shoulder can be a result of various additional processes. One explanation could be an emergence of an extra transition occurring with the band-band transition thus indicating an existence of an additional state. An alternative approach would argue for reabsorption which has been observed for direct bandgap and high quality semiconductors like perovskites [28]. However, to make any conclusions of this observation, further investigations and measurements on more samples would have to be done.

Before considering any possible physical explanations of the emission wavelength blue-shift with increasing nanowire diameter of the samples, our centre peak values should be put into perspective. The emission wavelengths observed for our samples were generally

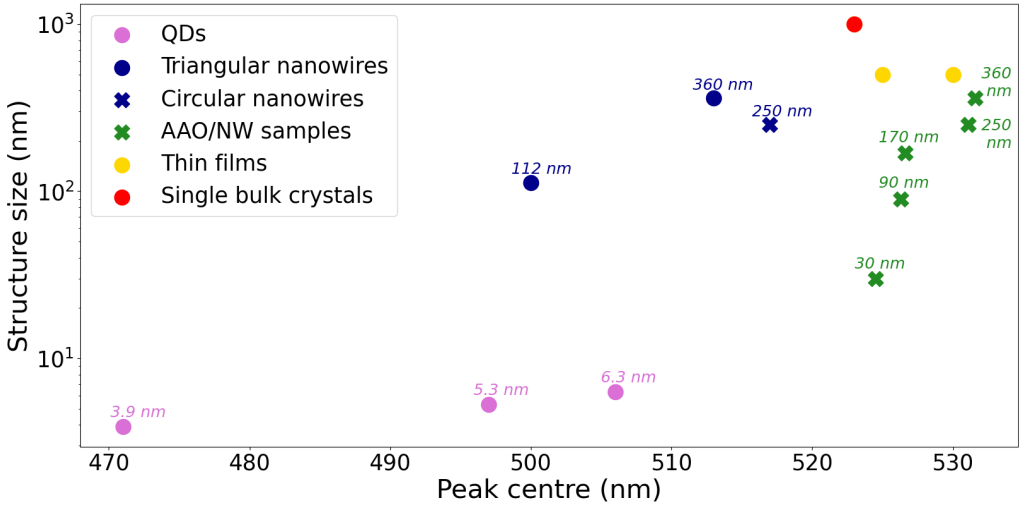

Figure 4.2: Comparison of the PL emission of different $CsPbBr_3$ structures, including QDs [34], triangular NWs [30], single circular nanowires pulled out from our AAO template, thin films [19, 40] and a bulk single crystal [32] to the samples studied here (AAO samples).

longer compared to horizontally laying NWs and even single bulk crystal measured under similar conditions as shown in the plot in Fig. 4.2. The emission from our samples showed a similar range of wavelengths as that of thin films with a thickness of less than 1 μm [19, 40]. Further, the emission of QDs ranging from 3.9 to 6.3 nm in size confirms a more energetic emission compared to our samples due to quantum confinement. This also results in more apparent blue-shift with decreasing size for the QDs. It is important to highlight that the circular NW which has a peak centre position around 517 nm represents an average value of three NWs which were pulled out from our 250 nm diameter sample and were measured at exactly the same conditions as the AAO/NW samples. This therefore strongly suggests that the PL emission of our samples could be affected by the interaction with the surrounding AAO matrix. The triangular nanowires mentioned here, grown on a C-plane sapphire substrate, show larger emission blue-shift due to lattice strain compared to the yet unexplained shifts seen for our AAO/NW samples [30].

The interpretation of the blue-shift of the emission wavelengths for our system can become very ambiguous. Noting that the Bohr-exciton radius of $CsPbBr_3$ is approximately 7.5 nm [20], quantum confinement effects can be in principle ruled out to be the origin of the size dependent PL observed. Another phenomena which one consults when a variation in emission of semiconductor nanostructures is observed is the Varshni effect. The Varshni

effect describes the dependence of a bandgap size on temperature, where for perovskites one expects a larger bandgap with higher temperature [3]. As stated by Oksenberg et al. [20], larger NW diameter would imply increased local heating of the nanowire and thus a blue-shift with increasing NW diameter would be expected. This is, however, not the case and thus any thermal effects can be ignored to be the cause. Moreover, an X-ray powder diffraction (XRD) measurement, briefly explained in Appendix A, at room temperature of all samples was performed by my colleague Zhaojun Zhang where all samples demonstrated an orthorhombic lattice. Therefore a change the PL emission due to the change of crystal structure could be excluded as well.

A possible explanation for the blue emission shift, could be the strain exerted on the the crystal lattice as diameter increases. As mentioned, changes in band gap of $CsPbBr_3$ NWs can be observed due to lattice rotations which cause a tilting of the perovskite octahedron and in turn alter the electron orbital overlap resulting in bandgap modulations [30]. Even though our emission data shows a similar trend, the NWs studied by Oksenberg et al. [30] have slightly different geometry and the strain induced by the substrate is only acting in one dimension while in our case we could speak of a radial strain effect instead. Therefore a further investigation would be necessary for a confirmation of this hypothesis.

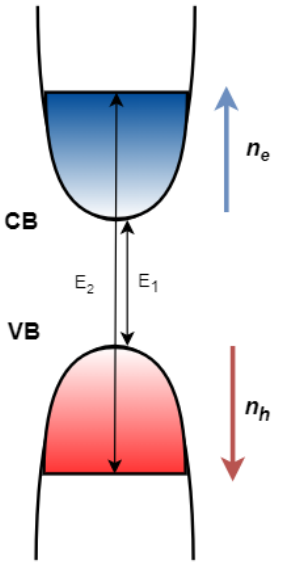

Figure 4.3: Band filling as charge carrier densities n_h and n_e increase.

An alternative explanation could be the band filling effect, also known as Moss-Burstein effect, which is outlined in Fig. 4.3. Band filling occurs when the electron and hole densities, n_e and n_h, increase leading to filling up the near band edge states. As all fermions must obey the Pauli exclusion principle, this leads to the occupation of higher states and consequently results in the emission of higher energetic photons with energy E_2 as shown in Fig. 4.3 [5]. In practise, it would mean that more spatially confined NWs have higher charge carrier densities which lead to filling up of the lower, near-band-edge energy states and thus smaller diameter NWs should have more energetic emission. However, observations of Moss-Burstein effect have not been confirmed on any similar systems

therefore stain effects seem to be the most plausible cause of the blue-shift in the case of our samples.

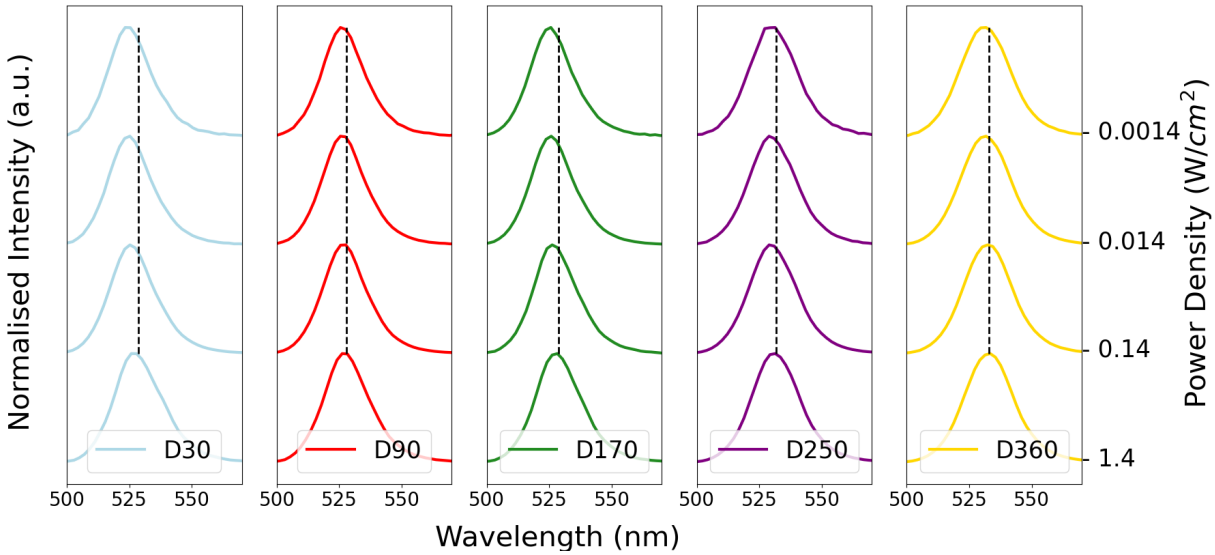

Figure 4.4: PL emission dependence on the excitation power density measured with 80 MHz repetition rate where the vertical dashed lines indicate the centre position of peaks at highest power density.

When exploring the power dependence of the emission wavelength, significantly longer wavelengths were observed with increasing excitation power density as shown in Fig. 4.4. The power dependent change in emission wavelength was more considerable for samples with smaller diameters (D30-D170) which is highlighted in Fig. 4.5 a). However, all samples exhibited a red-shift at increased excitation power density. A general trend could not be concluded for the FWHM as a function of excitation power density. As shown in Fig. 4.5 b), the behaviour was completely different for samples D30 - D170 and D250 - D360. Samples with diameter 30-170 nm showed an increase in FWHM with a higher excitation power density while in the case of samples with 250 nm and 360 nm diameters, the FWHM was smaller for higher excitation power densities. It should be noted that for all samples at all excitation power densities, the FWHM values are 5-10 nm larger than those reported by literature [20, 25, 38] suggesting an overall lower crystal quality.

It should be noted that the results of the power dependence of emission wavelength could be affected by the distinct light absorption resonances of the NWs with different diameters. As demonstrated by Attu [13] in a theoretical study on InP NWs, the absorption

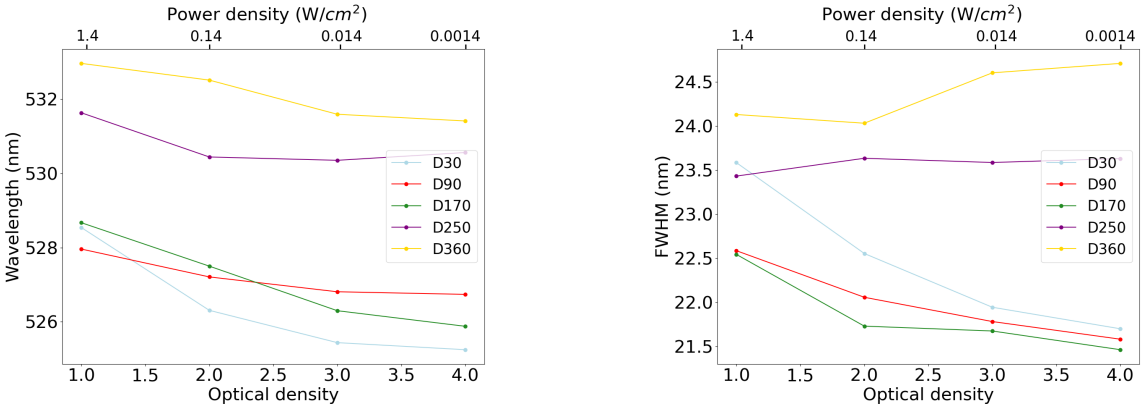

Figure 4.5: The emission wavelength (a) and FWHM (b) of the spectral peaks as a function of filter optical density and excitation power density for all diameters measured with 80 MHz repetition rate.

mechanisms of NWs can be based on the ratio between the excitation wavelength and NW diameter. The optimal absorption via so-called nanophotonic resonances occurs when the NW diameter approaches the excitation wavelength. As the excitation wavelength used in our measurements was 485 nm, samples with larger diameter should theoretically have stronger absorption at all excitation powers. Therefore for smaller diameter samples, with the same logic in mind, this would mean lower absorption which could further imply a larger difference between emission wavelengths at higher and lower excitation power densities for a particular small diameter sample.

As discussed, the emission wavelength of all samples was red-shifted with increasing power density. Such a result is very unintuitive as one would expect a blue-shift of the emission with the increasing excitation power density due to two usual effects; local heating of samples and band filling. (i) The local heating of the sample which could induce larger bandgap with increasing temperature (achieved with higher excitation power) as described by Varshni effect mentioned earlier. (ii) The band filling effect as the charge carrier densities n_e and n_h are expected to increase with higher excitation power density. In both cases one would expect a blue-shift with increasing power density thus neither of these effects can explain the observations.

4.1.2 PL Surface Density

To get a sense of the variation of the PL emission intensities of the different samples, PL images of the samples' cross-sections were taken and PL surface density was obtained via image integration. Looking at Fig. 4.6, one can see that the PL surface density is approximately the same for all samples with variations no greater than a factor of two. With this simplistic view, one can conclude that the size of the diameter most probably does not alone affect the crystal quality of the embedded nanowires as the intensity of the emitted PL is roughly of the same order of magnitude. However, an accurate analysis of the emitted PL which considers the number of photons absorbed by the material and the number of photons reaching the material, such as PLQY measurement, is required to make concrete conclusions.

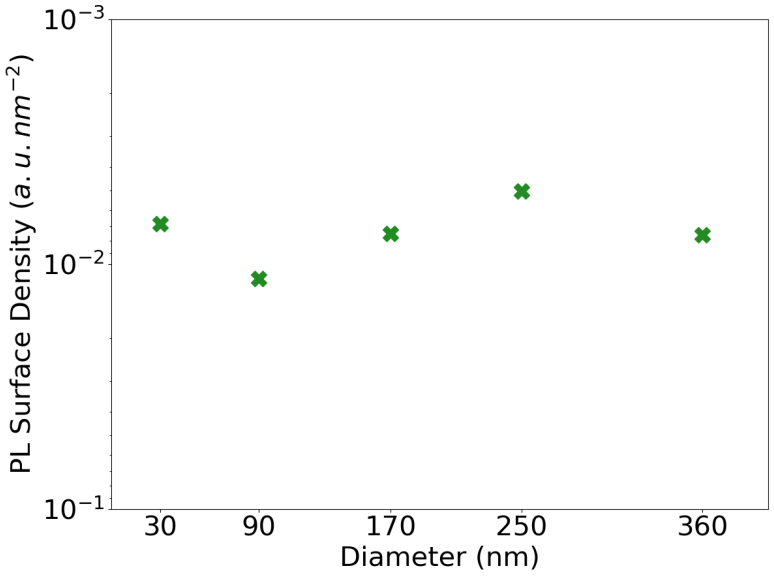

Figure 4.6: Photoluminescence surface density measured from the cross-section of the samples plotted on a log scale where repetition rate of 80 MHz and excitation power density of 0.0014 W cm^2 were used for the measurement.

4.2 Time-resolved PL

4.2.1 Dependence of PL Decay on Pore Diameter and Excitation power

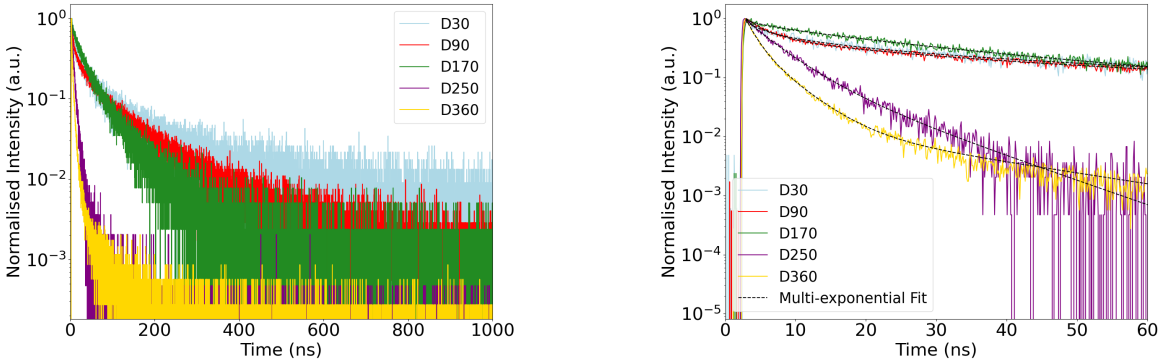

(a) (b)

Figure 4.7: PL decays of D30-D360 samples measured with a 0.014 W/cm^2 excitation power density (low power density regime) acquired for 100s with 500 kHz repetition rate where (a) shows a large window of the decay curves, (b) shows an enlarged part of the curves fitted with a multi-exponential function.

The decay measurements were done from a clean cross-section to avoid any interference of surface impurities, such as surface solids, with the PL from the actual NWs. The decays of the samples were observed to shorten with increasing NW diameter as presented in Fig. 4.7. When fitting the decay curves with Eq. (2.4), three different decay time components, τ_1, τ_2 and τ_3 with three different amplitudes were obtained for each sample. This data is collective summarised in Fig. 4.8 a) together with an average decay value for each sample. From the figure, it is even more apparent that the decay times are greatly varying between the small diameter, D30-D170, and the large diameter, D250-D360, samples. To get an even more concrete picture on the decay time variation, the average decays obtained are collected in Table 4.2 and further details such as the values of each respective decay components and their amplitudes can be found in Appendix C.

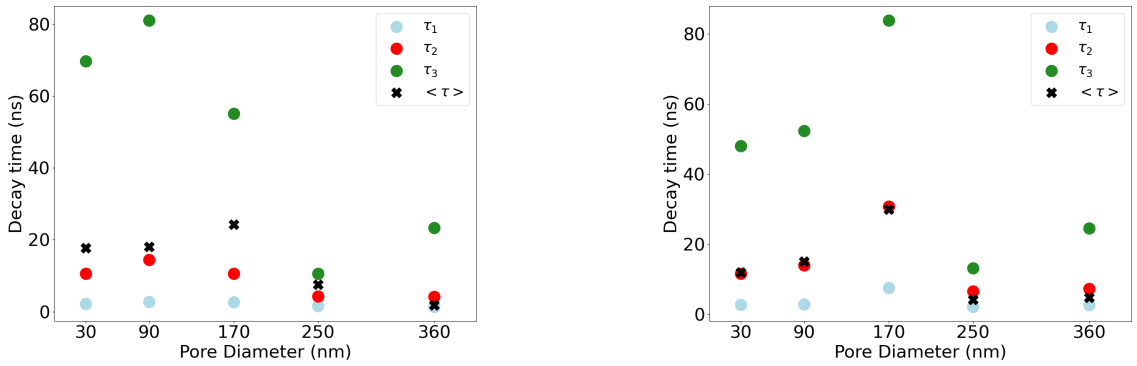

Figure 4.8: A scatter plot of the three components of the decay time obtained for all samples with a highlighted average decay time measured with 500 kHz repetition rate and (a) 0.014 W/cm^2 and (b) 1.4 W/cm^2 excitation power densities.

The dependence of the charge carrier decay kinetics on the excitation power density was explored by comparing the decays at low and high excitation power densities. The general decay dependence on the pore diameter remained the same when the excitation power was increased from 0.014 W/cm^2 to 1.4 W/cm^2 by changing from the excitation filter from OD3 to OD1 as demonstrated by the trend of the decay curves in Fig. 4.9. The extracted decay times, plotted in Fig. 4.8 b) show a similar trend as the one seen at lower excitation power density with a slight lower spread of the decay times between the samples. Conclusively, the samples with smaller diameter continue to prove to have much longer decay (3-9 times) even at higher excitation power densities as can be seen from Table 4.2.

Table 4.2: Summary of the decay times obtained by multi-exponential fitting of the curves in Fig. 4.7 (b) and Fig. 4.9 (b) of all samples measured at low and high power densities where$\langle\tau_{LP}\rangle$ and $\langle\tau_{HP}\rangle$ are the average decay times at low and high excitation power densities, respectively.

Sample D [nm]	$\langle\tau_{LP}\rangle$[ns]	$\langle\tau_{HP}\rangle$[ns]
30	17.7	12.0
90	18.0	15.1
170	24.3	29.9
250	7.6	4.1
360	1.8	4.8

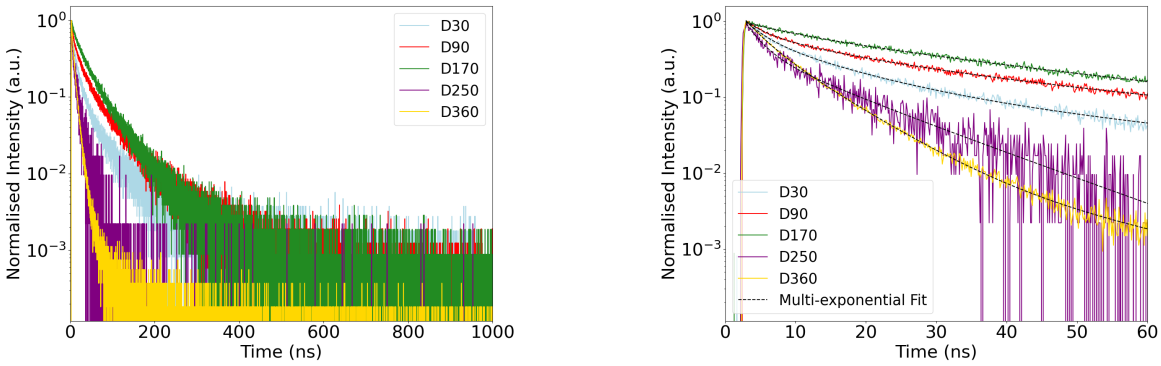

(a) (b)

Figure 4.9: PL decays of D30-D360 measured with 1.4 W/cm^2 excitation power density for 50s with 500 kHz repetition rate where (a) full decay curve (b) enlarged and fitted part of the curve.

The large difference between the decays of smaller diameter, D30-D170 samples and the larger diameter, D250-D360, samples suggests a very different charge carrier dynamics in the two cases. The reasoning for treating the smaller and larger diameter samples as two separate cases is further supported by the different behaviour of their PL emission described in the previous section. Our current hypothesis for such a behaviour is based on a trap-mediated carrier PL of the smaller diameter samples. The anticipated higher defect density can lead to a trapping-detrapping mechanism where the charge carriers are prevented from recombining radiatively. The decrease in decay time with higher excitation power density in the D30 and D90 samples then suggests a saturation of the trap states which as a consequence then have effect on the PL dynamics. Further, the trapping of charge carriers could be the reason for the slow decay onset of small diameter samples visible for both high and low excitation power densities. The trapping of the carriers then corresponds to a sudden change in the gradient of the decay curve, mostly visible in Fig. 4.7. Such an effect can be thus referred to as "delayed" luminescence which causes the observed seemingly long-lived states.

Following the results of Oksenberg et al. [30], the origin of the higher density of trap states could be attributed to a general higher distortion of the crystal structure caused by larger strain effects due to the confinement of the NWs by the AAO matrix. Such a distortion could cause a discontinuity of energy bands and thus also affect the PL emission wavelength. Furthermore, the higher surface to volume ratio of the smaller diameter samples entails a larger effect of the interaction between the NWs and the AAO template on the charge dynamics as well as the PL emission.

Lastly, coming back to the question of the nature of charge carriers in perovskites stated in the *scientific background chapter*, one can draw a confirmation of the anticipated free charge carrier majority. As when a semiconductor with a majority of stable excitons with $E_B > k_B T$ is considered, one does not observe a dependence of its radiative decay time on the charge carrier densities, i.e excitation power density. As a variation of decay times is observed for all samples studied here thus free charge carriers present the majority of carriers upon photoexcitation.

4.2.2 Bright and Dark Spots on Sample Surface

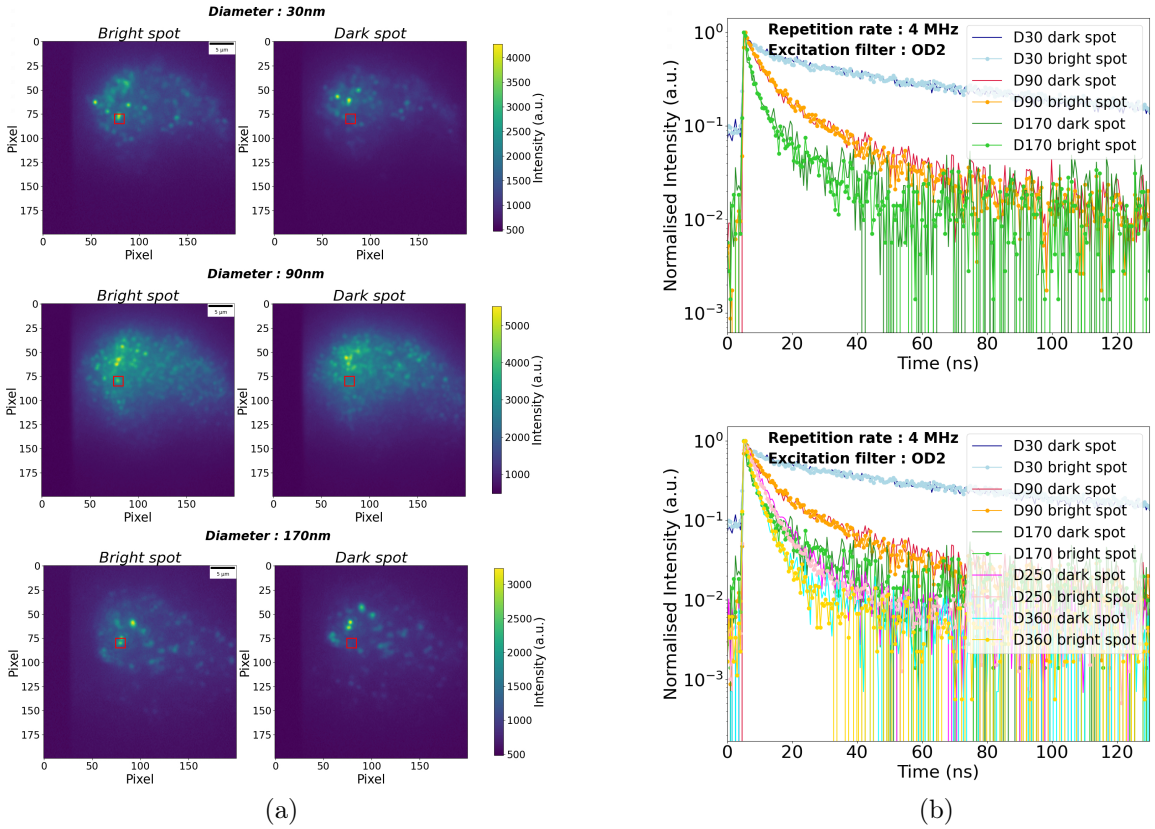

(a) (b)

Figure 4.10: Comparison of the decay times of dark and bright spots on D30-D170 nm samples measured with a 4MHz repetition rate and 0.14 W/cm^2 excitation power density, (a) PL images with a highlighted spot of TCSPC measurement (b) top: comparison of decay times for bright and dark spots for D30-D170 samples, bottom: comparison of decay times of bright and dark spots for D30-D360 samples.

After observing some deviations in the emission spectra taken from the top of the samples, it was investigated whether dark and bright domains observed represented a quality gradient of the material or simply indicated the amount of material in the pores. For each sample, decay measurements with accumulation time of 60s were done for pairs of neighbouring bright and dark spots to ensure the in-homogeneity of the samples did not affect the results. As shown in Fig. 4.10 b) and Fig. 4.11 b), the slopes of the decay curves are nearly identical and thus so are the decay times. Therefore, it could be concluded that the difference in PL emission intensity is caused by different amounts of the $CsPbBr_3$ perovskite in the pores.

However, it is important to point out that the dark and bright spots possibly represent nanowire domains rather than single nanowires due to a limited resolution of 200 nm of the setup.

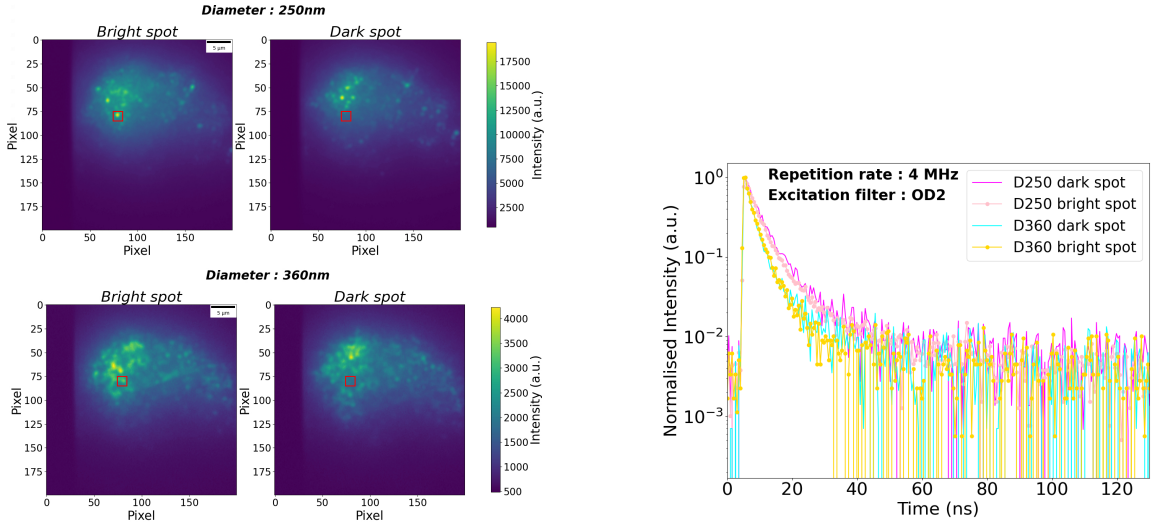

(a) (b)

Figure 4.11: Comparison of the decay time of dark and bright spots on D250-D360 nm samples, (a) PL images with a highlighted spot of TCSPC measurement (b) comparison of decay times for bright and dark spots for D250-D360 samples.

Chapter 5

Conclusion and Outlook

With the novel approach of employing AAO templates as a physical support for solution-processed $CsPbBr_3$ NWs used for photodetection purposes, further questions arise regarding the optical properties of such NWs. With the help of steady-state and time-resolved PL techniques, clarifications regarding the type of photocarriers in $CsPbBr_3$, the PL emission properties as well as charge carrier dynamics could be made. The observation of blue-shift with decreasing nanowire diameter size was attributed to possible strain effects on the crystal lattice induced by the AAO matrix. While band-filling was considered as a second less probable origin.

When looking at the PL surface density, all samples showed very similar brightness levels with variations of no more than a factor of two. Nevertheless, a comprehensive PLQY measurement would need to be done to confirm with certainty the prediction of the approximation. Moreover, as PLQY is one of the crucial quantities for the evaluation material's scintillation properties, such as the *conversion efficiency* η, the execution of such measurement is indeed necessary. The answering of the question regarding the sample with the utmost suitability for a scintillator, gained complexity with the inclusion of time-resolved measurement results. The TCSPC measurement revealed abruptly short decay times for the charge carrier population in the large diameter samples. The variation between D30-D170 and D250-D360 decay times was as large as a factor of nine. The significantly longer decay times of D30-D170 samples were hypothesised to correspond to a trap-mediated PL mechanism. Taking into account both the steady-state and time-resolved measurements obtained so far, the samples with the larger pore diameter present

themselves as better candidates for X-ray scintillation detection due to their shorter decay times.

The majority of the charge carriers in the samples was identified to be free charge carriers. However, to understand the complete nature of the charge carriers in $CsPbBr_3$, a temperature dependent steady-state and time-resolved PL would be required to get a better insight on the photophysics which could aid with drawing a concrete picture. As free exctions tend to resonate through the lattice of a material while reabsorbing the PL photon, the PL emission will almost never occur (unless at very low T) and will thus not be visible in the emission spectra. On the other hand, absorption measurements would clearly reveal any excitions present in the material.
Lastly, as the samples showed an in-homogenity to a certain extend and taking into account the given infamous instability of perovskites, investigation of multiple sets of the samples could improve not only the reliability of the measurements but also give a better understanding on the decay and emission size related trends.

Bibliography

[1] M. N. Saha. "On a physical theory of stellar spectra". In: *Proceedings of the Royal Society of London* 5 (1921), pp. 135–153.

[2] B. Nam net al. "Free-exciton energy spectrum in GaAs". In: *Phys. Rev. B* 13.761 (1976).

[3] X. Chen K. P. O'Donnell. "Temperature dependence of semiconductor band gaps". In: *Appl. Phys. Lett.* 58 (1991).

[4] C. C. Phillips P. J. P. Tang M. J. Pullin. "Binding energy of the free exciton in indium arsenide". In: *Phys. Rev. B* 55 (1997).

[5] J. Monecke P. Verma G. Irmer. "Laser power dependence of the photoluminescence from CdSxSe1-x nanoparticles in glass". In: *J. Phys.: Condens. Matter* 12 (2000).

[6] S. Rein. *Lifetime spectroscopy: A method of defect characterization in silicon for photovoltaic applications.* New York, USA: Springer, 2005.

[7] J. R. Lakowicz. *Principles of Fluorescence Spectroscopy.* 3rd ed. New York,USA: Springer, 2006.

[8] M. Nikl. "Scintillation detectors for X-rays". In: *Meas. Sci. Technol* 17 (2006), R37–R54.

[9] S. Billinge R. E. Dinnebier. *Principles of Powder Diffraction.* Cambridge : Royal Society of Chemistry, 2008.

[10] S. Lanceros-Mendez J. G. Rocha. "Review on X-ray Detectors Based on Scintillators and CMOS Technology". In: *Recent Patents on Electrical Engineering* 4 (2011).

[11] J. Valenta I. Pelant. *Luminescence Spectroscopy of Semiconductors.* UK: Oxford University Press, 2012.

[12] M. F. L'Annunziata. *Handbook of Radioactivity Analysis*. 3rd ed. USA: The Montague Group, 2012. Chap. 16. Solid Scintillation Analysis.

[13] N. Anttu. "Geometrical optics, electrostatics, and nanophotonic resonances in absorbing nanowire arrays". In: *Optics Letters* 38 (2013).

[14] V. D'Innocenzo et al. "Excitons versus free charges in organo-lead tri-halide perovskites". In: *Nature Communications* 5 (2014).

[15] M. Wahl. *Time-Correlated Single Photon Counting*. Tech. rep. Rudower Chaussee 29, 12489 Berlin, Germany: PicoQuant GmbH, 2014.

[16] W. Becker. *Advanced Time- Correlated Single Photon Counting Applications*. Switzerland: Springer, 2015.

[17] M. J. Ashley et al. "Templated Synthesis of Uniform Perovskite Nanowire Arrays". In: *J. Am. Chem. Soc.* 138 (2016), 10096-10099.

[18] N. Das P. Bhardwaj. "Exciton binding energy in bulk and quantum well of semiconductors with non-parabolic energy bands". In: *IJESRT* 5 (2016), pp. 289–294.

[19] S. Li Y. Li Z. Shi. "High-performance perovskite photodetectors based on solution-processed all-inorganic CsPbBr3 thin films". In: *J. Mater. Chem. C* 5 (2017), pp. 8355–8360.

[20] E. Oksenberg et al. "Surface-Guided CsPbBr3 Perovskite Nanowires on Flat and Faceted Sapphire with Size-Dependent Photoluminescence and Fast Photoconductive Response". In: *Nano Lett.* 18 (2018), pp. 424–433.

[21] K. Hong et al. "Low-dimensional halide perovskites: review and issues". In: *J. Mater. Chem. C* 6 (2018), pp. 2189–2209.

[22] T. Qiu et al. "Recent advances in one-dimensional halide perovskites for optoelectronic applications". In: *Nanoscale* 10 (2018), pp. 20963–20989.

[23] J. Cheng. "Photophysics of Perovskite Nano- and Microcrystals". PhD thesis. Lund University,Faculty of Science, Department of Chemistry, Division of Chemical Physics, Feb. 2018.

[24] A. Ul-Hamid. *A Beginners' Guide to Scanning Electron Microscopy*. Springer, Cham, 2018.

[25] A. K. Jena et al. "Halide Perovskite Photovoltaics: Background,Status, and Future Prospects". In: *Chem,Rev.* 119 (2019), pp. 3016–3103.

[26] L. Wang et al. "A Eu3+-Eu2+ ion redox shuttle imparts operational durability to Pb-I perovskite solar cells". In: *Science* 363 (2019), pp. 265–270.

[27] S. Bai et al. "Planar perovskite solar cells with long-term stability using ionic liquid additives". In: *Nature* 363 (2019), pp. 245–250.

[28] D. Emin D. W. deQuilettes K. Frohna. "Charge-Carrier Recombination in Halide Perovskites". In: *Chem. Rev.* 119 (2019), 11007-11019.

[29] A. Pan Y. Jiang X. Wang. "Properties of Excitons and Photogenerated Charge Carriers in Metal Halide Perovskites". In: *Adv. Mater.* 31 (2019).

[30] E. Oksenberg et al. "Large lattice distortions and size-dependent bandgap modulation in epitaxial halide perovskite nanowires". In: *Nat. Commun.* 11 (2020).

[31] F. Zhou et al. "Halide Perovskite, a Potential Scintillator for X-Ray Detection". In: *Small methods* 4 (2020).

[32] G. Mannino et al. "Temperature-Dependent Optical Band Gap in $CsPbBr_3$, $MAPbBr_3$, and $FAPbBr_3$ Single Crystals". In: *J. Phys. Chem. Lett.* 11 (2020), pp. 2490–2496.

[33] J. Qin et al. "Carrier Dynamics and Evaluation of Lasing Actions in Halide Perovskites". In: *Trends in Chemistry* https://doi.org/10.1016/j.trechm.2020.10.010 (2020).

[34] O. H. Cheng et al. "Size- and temperature-dependent photoluminescence spectra of strongly confined CsPbBr3 quantum dots". In: *Nanoscale* 12 (2020).

[35] Q. Zhang et al. "Three-Dimensional Perovskite Nanophotonic Wire Array-Based Light-Emitting Diodes with Significantly Improved Efficiency and Stability". In: *ACS Nano* 14 (2020), pp. 1577–1585.

[36] Y. Jiang et al. "Photoluminescence Mechanisms of All-Inorganic Cesium Lead Bromide Perovskites Revealed by Single Particle Spectroscopy". In: *ChemNanoMat* 6 (2020), pp. 327–335.

[37] Y. Liu et al. "Multilayerd 2D Cesium-Based Hybrid Perovskite with Strong Polarization Sensitivity: Dimensional Reduction of $CsPbBr_3$". In: *Chem. Eur. J.* 26 (2020), pp. 3494–3498.

[38] Z. Zhang et al. "Air-stable vertically aligned $CsPbBr_3$ nanowires arrays with confinement induced crystal phase transition". In: *Manuscript* (2020).

[39] A. K. Chauhan P. Kumar. "Highly efficient flexible perovskite solar cells and their photo-stability". In: *J. Phys. D: Appl. Phys* 53 (2020).

[40] W. Feng R. Chena Z. Lianga. "Solution-processed all-inorganic perovskite CsPbBr3 thin films for optoelectronic application". In: *Journal of Alloys and Compounds* https://doi.org/10.1016/j.jallcom.2020.158125 (2020).

[41] A. Majcher M. Lacarra. EU-HOU project;Université Pierre et Marie Curie, Center for Theoretical Physics PAS.

Appendix A

Additional Characterisation Techniques

Scanning Electron Microscopy

Scanning electron microscopy (SEM) is an imaging characterisation technique which uses a beam of highly energetic electrons to scan the surface of a conducting sample. As the wavelength of the electrons is far smaller than that of visible light, features beyond the nanometer range can be resolved with SEM. A typical SEM consists of an electron gun, where electrons are generated, and a system of electromagnetic lenses which merge the electrons into a focused beam. The scanning of the electron beam across the sample is then facilitated by a pair of scanning coils. The electrons from the beam interact with atoms located within a few μm below the surface of the sample. As a result of the interaction, a variety of signals, such as secondary electrons, X-rays and back-scattered electrons, are produced giving different information about the sample's surface upon detection. The images included in this work were made with a Hitachi SU8010 Cold Field Emission instrument using the secondary electron signal. [24]

X-ray Powder Diffraction

X-ray powder diffraction technique gives insight on the structure of the crystal lattice of a particular material. The technique is based around the fundamental theory of diffraction, the Bragg's law. When X-rays interact with the ordered structure of a crystalline material, they scatter and interfere giving rise to constructive and destructive interference. A crystal structure specific diffraction patter is thus produced. [9]

Appendix B

Filter Parameters

B.1 Cube for the 485 nm Laser

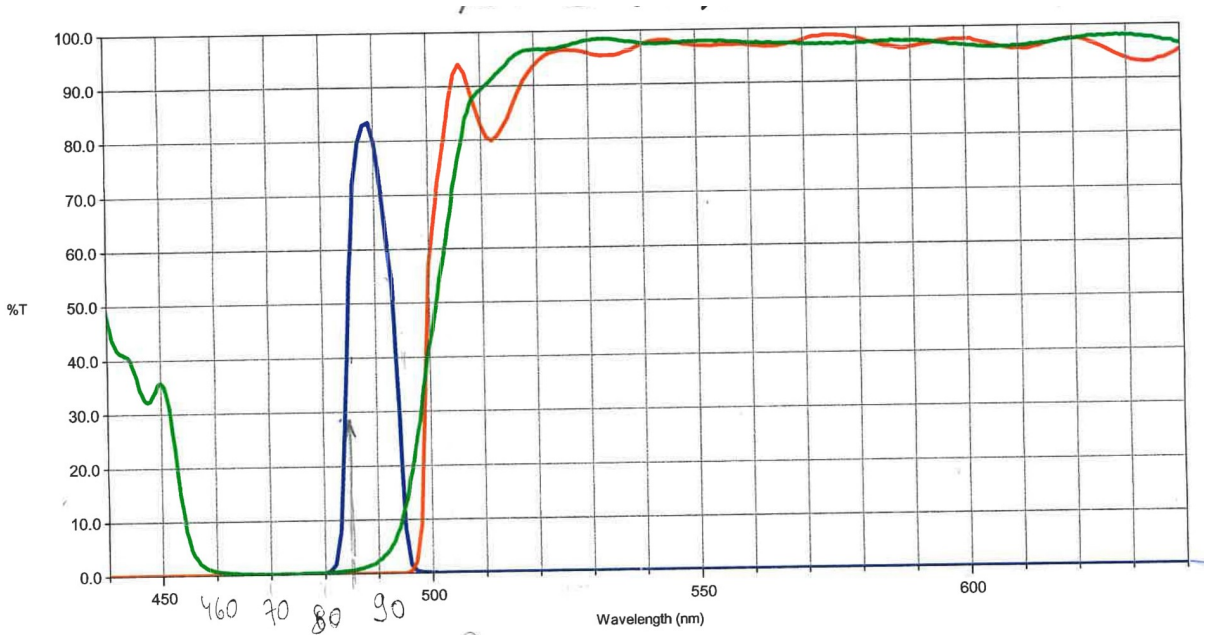

Figure B.1: Transmission functions for the cube used for the 485 nm diode laser where green is the dichroic mirror, blue is the clean-up filter and red is the LP emission filter.

Appendix C

Decay Fit Values

Table C.1: Summary of the fitted values in multi-exponential fits of charge carrier decay curves for the data obtained at low excitation power density.

Parameter	D30	D90	D170	D250	D360
α_1	1.00± 0.07	1.41± 0.02	0.36 ±0.08	0.8±0.2	5.00±0.05
τ_1	2.18±0.02	2.765±0.001	2.63±0.01	1.54±0.03	1.37±0.03
α_2	0.4±0.2	0.30±0.05	0.5±0.1	1.4±0.2	0.8±0.2
τ_2	10.5±0.1	14.47±0.02	10.5±0.1	4.3±0.3	4.2±0.3
α_3	0.35±0.03	0.28±0.02	0.4±0.1	0.2±0.1	0.02±0.01
τ_3	69.631±0.001	81.00±0.01	55.005±0.003	10.53±0.02	23.34±0.02

Table C.2: Summary of the fitted values in multi-exponential fits of charge carrier decay curves for the data obtained at high excitation power density.

Parameter	D30	D90	D170	D250	D360
α_1	1.14±0.03	0.93±0.02	0.4±0.5	2.0±0.3	1.25±0.05
τ_1	2.77±0.01	2.80±0.01	7.46±0.02	2.1±0.4	2.62±0.01
α_2	0.59±0.04	0.48±0.04	0.7±0.1	0.2±0.2	0.91±0.04
τ_2	11.60±0.02	13.97±0.02	30.77±0.03	6.6±0.1	7.27±0.02
α_3	0.15±0.02	0.32±0.03	0.1±0.6	0.4±0.6	0.02±0.01
τ_3	48.077±0.002	52.356±0.001	83.89±0.03	13.1±0.6	24.57±0.01

Appendix D

Fluorescence Lamp Spectrum

Table D.1: Identified peaks in the calibration spectrum in Fig. 3.8.

Peak Number	Wavelength [nm]	Element
2	436.6	Mercury
3	487.7	Terbium
4	542.4	Terbium
5	546.5	Mercury
8	584.0	Terbium/Europium
9	587.6	Europium
12	611.6	Europium
14	631.1	Europium
15	650.8	Europium
16	662.6	Europium
17	687.7	Europium
18	693.7	Europium
19	709.0	Europium
20	712.3	Europium

Appendix E

Analysis Code

E.1 PL Emission Spectra

```
############################### Libraries needed ################################

import numpy as np
import matplotlib.pyplot as plt
import scipy.optimize as opt
from tabulate import tabulate

############################## Importring data files ############################
#D30
path1=r'C:\Users\klark\Documents\Master_thesis\Data\2020-10-05\D30.spe'
path2=r'C:\Users\klark\Documents\Master_thesis\Data\2020-10-24\D30.spe'
#D90
path3=r'C:\Users\klark\Documents\Master_thesis\Data\2020-09-10\D90.spe'
path4=r'C:\Users\klark\Documents\Master_thesis\Data\2020-10-24\D90.spe'
#D170
path5=r'C:\Users\klark\Documents\Master_thesis\Data\2020-09-10\D170.spe'
path6=r'C:\Users\klark\Documents\Master_thesis\Data\2020-10-24\D170.spe'
#SINGLE WIRE
path7=r'C:\Users\klark\Documents\Master_thesis\Data\single_wire_PL.spe'
#D250
path8=r'C:\Users\klark\Documents\Master_thesis\Data\2020-10-05\D250.spe'
path9=r'C:\Users\klark\Documents\Master_thesis\Data\2020-10-24\D250.spe'
#D360
path10=r'C:\Users\klark\Documents\Master_thesis\Data\2020-10-05\D360.spe'
path11=r'C:\Users\klark\Documents\Master_thesis\Data\2020-10-24\D360.spe'
```

```
def load_spe(foldername):#This function was written by Jun Li
    with open(foldername,'rb') as fid:
        header=fread(fid,2050,dtype=np.uint16)
        Xdim=np.double(header[21])
        Ydim=np.double(header[328])
        Zdim=np.double(header[723])
        MG=header[2048]
        DataType=header[54]
        if DataType==0:
            ImMat=fread(fid,-1,dtype=np.float32)
        elif DataType==1:
            ImMat=fread(fid,-1,dtype=np.int32)
        elif DataType==2:
            ImMat=fread(fid,-1,dtype=np.int16)
        else:
            ImMat=fread(fid,-1,dtype=np.int16)

        a=np.reshape(ImMat,(Zdim.astype(np.int64),Ydim.astype(np.int64),
                            Xdim.astype(np.int64)))
    C=np.double(a)

    return C
##################################FITTING PROCEDURE#############################
#Gaussian function to be used for fitting
def gaussian(xx, center, width, amplitude):
    yy = amplitude * np.exp(-4 * np.log(2) * (xx - center) ** 2 / width ** 2)
    return yy
#Function that calculates a sum of Gaussians and generates an array for values
#of the fitting to be stored
def gaussian_sum(xx, pp):
    npeaks = int((len(pp) - 1) / 3)#calculating total number of peaks
    #array which stores values of the Gaussian fitting
    yy = np.ones(len(xx)) * pp[-1]
    for ii in range(0, npeaks):
        yy += gaussian(xx,
                       pp[3 * ii],
                       pp[3 * ii + 1],
                       pp[3 * ii + 2])
    return yy
#Fuction calculating the difference between the fit and the data
def residuals(pp, xx, yy):
    rr = gaussian_sum(xx, pp) - yy
    return rr

###################### Fitting parameters to be obtained saved here#############
X_final=[]
Diameter=["Diameter / nm",30,30,90,90,170,170,"NW",250,250,360,360]
Lambda=["Emission wavelength /nm"]
FWHM=["FWHM / nm"]
############################ Intial guesses for fitting#########################
p0 = np.array([525, 1, 1,   #1st diffraction peak(peak cetre, width, amplitude)
               0.5,1.0,0.1,#0th difzdgfraction peak(peak cetre, width,
                           #amplitude)
              0.0]) # background value
```

```
##################################Gaussian fitting#############################
for i in range(len(YY)):
    fit_data = opt.leastsq(residuals, p0, args=(X[i], Y[i]), full_output=False)
    opt_parameters = fit_data[0]#selecting parameters of interest
    shift=opt_parameters[3]#centre of the 0th order peak
    x_corr=X[i]-shift#shifting the 0th order peak to zero
    X_final.append(x_corr)#saving the updated x-corrdinates for plotting
    exc=round(opt_parameters[0]-shift,2)# Emission wavelength
    Lambda.append(exc)
    k=round(opt_parameters[1],3)# FWHM
    FWHM.append(k)
#################### Saving data to table in a txt file ######################
Table=tabulate([Diameter,Lambda,FWHM],tablefmt="fancygrid")
with open(r'C:\Users\klark\Documents\Master_thesis\Data\Fitting_data.txt',
          mode='w')
     as fout_data:
    fout_data.write(Table)
############################## Plot all spectra ###############################
fig=plt.figure(figsize=(13,12))
lw=3
ax=fig.add_subplot(111)

#D30
ax.plot(X_final[0],Y[0],color='lightblue',linewidth=lw, label='D30')
ax.plot(X_final[1],Y[1],color='lightblue',linewidth=lw,label='D30')
#D90
ax.plot(X_final[2],Y[2],color='red',linewidth=lw, label='D90')
ax.plot(X_final[3],Y[3],color='red',linewidth=lw, label='D90')
#D170
ax.plot(X_final[4],Y[4],color='forestgreen',linewidth=lw, label='D170')
ax.plot(X_final[5],Y[5],color='forestgreen',linewidth=lw, label='D170')
#D250
ax.plot(X_final[7],Y[7],color='purple',linewidth=lw, label='D250')
ax.plot(X_final[8],Y[8],color='purple',linewidth=lw, label='D250')
#360
ax.plot(X_final[9],Y[9],color='gold',linewidth=lw, label='D360')
ax.plot(X_final[10],Y[10],color='gold',linewidth=lw, label='D360')

ax.set_xlabel('Wavelength (nm)',size=35)
ax.set_ylabel('Normalized Intensity (a.u.)',size=35)
leg = ax.legend(prop={"size":30});
ax.set_xlim([500,570])
ax.tick_params( labelsize=35)
plt.show()
```

E.2 PL Decay

```
############################## libraries needed ##############################
import matplotlib.pyplot as plt
import numpy as np
from scipy import stats

########################### loadidng data files ##############################
#30
data1=np.loadtxt( r'C:\Users\klark\Documents\Master_thesis\Data\2020-11-15\D30
                 ,skiprows=10,)
#90
data2=np.loadtxt( r'C:\Users\klark\Documents\Master_thesis\Data\2020-11-15\D90
                ,skiprows=10,)
#170
data3=np.loadtxt( r'C:\Users\klark\Documents\Master_thesis\Data\2020-11-15\D170
                ,skiprows=10,)
#250
data4=np.loadtxt( r'C:\Users\klark\Documents\Master_thesis\Data\2020-12-03\D250
                 ,skiprows=10,)
#360
data5=np.loadtxt( r'C:\Users\klark\Documents\Master_thesis\Data\2020-11-15\D360
                 skiprows=10,)
######################## Editing data files for fitting and ploting #############
DATA=[data1,data2,data3,data4,data5]
DATA_y=[]#adapted y-values
X=[]#adapted x-values
T=[]#decay times
Intercept=[]
Error=[]
R_value_sq=[]
for i in range (len(DATA)):
    c=DATA[i]
    b=sum(c[10145:15624])/(15624-10145+2)#calculating background in the tail
                                         #of the decay curve
    c1=c-b#substracting background
    I=max(c1)#finding maximum
    data_y=(c1/I)#normalising the data
    DATA_y.append(data_y)
    channel_time=0.1280###number of ns per bin
    x=(np.linspace(0,len(data_y)+1,len(data_y)))*channel_time
    X.append(x)
```

```
def _3exponential(x, a, k1,b,k2,c,k3):
    return a*np.exp(-x*k1) + b*np.exp(-x*k2)+ c*np.exp(-x*k3)
Error=[]
fit_param=[]
fit_param1=[]
pcov_param=[]

p0=[[0.5, 0.025, 0.89,0.31,0.5,0.01],[0.5, 0.04,0.2, 0.1,0.2,0.01],
    [0.5, 0.01,0.5, 0.1,0.5,0.01],[0.5, 0.01,0.5, 0.1,0.5,0.01],
    [0.5, 0.01,0.5, 0.1,0.5,0.01]]
for i in range(5):

    popt_3exponential, pcov_3exponential =
    scipy.optimize.curve_fit(_3exponential, X[i][23:790], Y[i][23:790],p0[i],
                             maxfev=100000,bounds=(0.00001,5))
    fit_param.append(popt_3exponential)
    pcov_param.append(pcov_3exponential)
    perr_3exponential = np.sqrt(np.diag(pcov_3exponential))
    Error.append(perr_3exponential)

#######################################Plotting#################################
fig=plt.figure(figsize=(13,12))
gs = gridspec.GridSpec(1,1)
ax1 = fig.add_subplot(gs[0])
without equations
ax1.plot(X[0],Y[0] , "lightblue",label="D30")
ax1.plot(X[1],Y[1] , "red",label="D90")
ax1.plot(X[2],Y[2] , "forestgreen",label="D170")
ax1.plot(X[3],Y[3] , "purple",label="D250")
ax1.plot(X[4],Y[4] , "gold",label="D360")

#30
ax1.plot(X[0][23:790], _3exponential(X[0][23:790],fit_param[0][0],
fit_param[0][1],fit_param[0][2],fit_param[0][3],fit_param[0][4],
fit_param[0][5]),
linestyle='dashed',color='black',label="Multi-exponential Fit")
#90
ax1.plot(X[1][23:790], _3exponential(X[1][23:790],fit_param[1][0],
fit_param[1][1],fit_param[1][2],fit_param[1][3],fit_param[1][4],
fit_param[1][5]), linestyle='dashed',color='black')
#170
ax1.plot(X[2][23:790], _3exponential(X[2][23:790],fit_param[2][0],
fit_param[2][1],fit_param[2][2],fit_param[2][3],fit_param[2][4],
fit_param[2][5]), linestyle='dashed',color='black')
#250
ax1.plot(X[3][23:790], _3exponential(X[3][23:790],fit_param[3][0],
fit_param[3][1],fit_param[3][2],fit_param[3][3],fit_param[3][4],
fit_param[3][5]), linestyle='dashed',color='black')
#360
ax1.plot(X[4][23:790], _3exponential(X[4][23:790],fit_param[4][0],
fit_param[4][1],fit_param[4][2],fit_param[4][3],fit_param[4][4],
fit_param[4][5]), linestyle='dashed',color='black')

ax1.set_xlim(0,60)
ax1.set_ylabel("Normalised Intensity (a.u.)",fontsize=30)
ax1.set_xlabel("Time (ns)",fontsize=30)
ax1.legend(loc=3,prop={"size":25})
plt.yscale('log')
ax1.tick_params( labelsize=30)
```